

ALMA MATER STUDIORUM · UNIVERSITY OF BOLOGNA

School of Science
Department of Physics and Astronomy
Master Degree in Physics

Fabrication and characterization of metal
halide perovskite-based memristors:
integration of an ionic buffer layer to control
the hysteretic behaviour

Supervisor:
Prof. Daniela Cavalcoli

Submitted by:
Martina Smacchia

Co-supervisor:
Prof. Antonio Guerrero
Dott. Lorenzo Maserati

Academic Year 2022-2023

Abstract

The intrinsic hysteresis of perovskites in the current-voltage response can be exploited for memory devices like memristors, which mimic brain-like synaptic functions and offer new computing possibilities. Since controlling the hysteresis is a fundamental point, the purpose of this work was to study the effect on the device response due to the integration of an ionic buffer layer in an already studied configuration. The memristor configuration considered as reference was FTO/PEDOT:PSS/MAPbI₃/Au. The material chosen for the buffer layer was poly(ethylene glycol) (PEG), doped with 1-butyl-3-methylimidazolium iodide (IL). Both the TOP configuration FTO/PEDOT:PSS/MAPbI₃/PEG+IL/Au, and the BOTTOM one FTO/PEG+IL/MAPbI₃/Au have been tested. In order to obtain a thin film of good quality, different solvents and concentrations of ionic liquid in the polymer have been tested, as well as different conditions for the layer deposition. Once the optimal conditions were found, the electrical response and the structure of the devices were studied. The device activation was studied via cyclic voltammetry, finding different behaviours in each of the three cases. In order to see morphological changes in the perovskite, Scanning Electron Microscopy was performed with secondary and backscattered electron detection, while Grazing Incidence Wide Angle X-Ray Scattering measurements allowed to determine structural changes and different crystallites orientation with respect to the reference case. The three different devices that have been tested showed significant differences. The BOTTOM device exhibited a larger hysteresis than the reference but it was not possible to deactivate it after the first cycle, and the perovskite crystallization appeared different in this case. A more interesting case is represented by the TOP device which was the only one exhibiting activation for negative voltage. Moreover, not only the functionality but also the perovskite crystalline structure was deeply modified by the presence of the buffer layer.

Contents

Abstract	i
List of Figures	vii
Introduction	1
1 Memristors	2
1.1 Types of memristive systems	5
1.1.1 Resistive Switching in ReRAM	6
1.2 Characteristics of Memory Devices	8
1.3 Comparison of Emerging Memory Technologies	8
1.4 Performance parameters of memristors	9
2 Hybrid perovskites	12
2.1 Crystal structure	13
2.1.1 Hysteresis and ionic transport	15
2.2 Stability issues	16
2.3 Perovskites in Memristor Technology	18
2.3.1 Switching mechanism	19
2.3.2 Application	20
3 Methods	22
3.1 Device fabrication	22
3.2 Device characterization	26
3.2.1 Cyclic voltammetry and retention measurements	26
3.2.2 Impedance Spectroscopy	27
3.2.3 Scanning Electron Microscope	29
3.2.4 Grazing Incidence Wide Angle X-ray Scattering	31
4 Results and Discussion	33
4.1 Introduction of the buffer layer	33
4.2 Electrical response	36

4.3	Impedance Spectroscopy	40
4.4	Grazing Incidence Wide Angles X-ray Scattering	42
4.4.1	Reference configuration: FTO/PEDOT:PSS/MAPI	43
4.4.2	Bottom configuration: FTO/PEG+IL/MAPI	45
4.4.3	Top configuration: FTO/PEDOT:PSS/MAPI/PEG+IL	47
	Conclusions	50
	Bibliography	51

List of Figures

1.1	Equivalent circuit describing the chemical inductor.	4
1.2	Illustration of the hysteresis loop of memristive devices when subjected to periodic stimulus, for both (a) “self-crossing” and (b) “not self-crossing” cases. [4]	5
1.3	Illustration of the two-terminal emerging memory technologies:(a) resistive random access memory (ReRAM), (b) phase change memory (PCM), (c) ferroelectric random access memory (FeRAM), and (d) spin-transfer torque magnetic random access memory (STT-MRAM). [4]	6
1.4	Representation of different I-V responses in ReRAM: (a) bipolar resistive switching and (b) threshold resistive switching. [4]	7
1.5	Typical I-V curve in semilogaritimic scale for a BRS type ReRAM device and performance parameters. [4]	10
2.1	Crystal structure of a cubic ABX ₃ perovskite. [4]	13
2.2	Rapresentation of the Goldschmidt’s tolerance factor a perovskite structure, where r_A , r_B , and r_X are the ionic radii of the A-,B-, and X-site atoms. [13]	14
2.3	Scan direction dependendace for the (a) normal-type hysteresis and (b) inverted-type hysteresis.	15
2.4	Scheme of three ionic transport mechanisms in MAPbI ₃ due to (a) I ⁻ , Pb ²⁺ and (b) MA ⁺ migration. [4]	15
2.5	Representation of the degradation mechanism induced by moisture in perovskite film. [17]	17
2.6	Representation of the three steps photo-oxidative process determining degradation in MAPbI ₃ (001) surface. [19]	18
2.7	Scheme of a perovskite-based memristors and different device configurations influencing the memristive response. [4]	19
2.8	Scheme of ABX ₃ perovskite based memristors with (a) nonfilamentary swtiching, and (b) filamentary swtiching mechanisms. [4]	20

3.1	Device configurations tested in this work:(a) no buffer layer (reference), (b) buffer layer on top of MAPI layer(top), (c) buffer layer below of MAPI layer (bottom).	22
3.2	cross section of the device in the "top" configuration at each step of the fabrication:(a) substrate (b) etched FTO, (c) pedot, (d) MAPI, (e) PEG+IL, (f) scratched substrate, (g)gold contacts	23
3.3	PEG solution preparation in IPA.	24
3.4	(a) Top view and (b) cross section of the 1x1 cm ² memristor configuration	25
3.5	Schematic diagram of the characteristic I V response and chronoamperometry measurement of memristors inside the nitrogen-filled glove box. .	26
3.6	(a) Series of voltages applied to the device, (b) definition of V_{READ} and V_{SET}	27
3.7	Schematic representation of the sample mounted on a mica substrate with copper contacts(a) and the experimental setup(b) for the impedance measurements using both the keysight LCR meter and the Autolab PGSTAT204.	28
3.8	(a) Equivalent circuit representative of a memristor and (b) equivalent circuit chosen to perform the impedance measurements with the LCR meter.	29
3.9	Scheme of a scanning electron microscope.	29
3.10	Sketch of the GIWAXS experiment geometry.	31
4.1	Comparison between the obtained films for different concentration of IL. The images, obtained with an optical microscope with 40x magnification, represent: (a) FTO substrate without PEG+IL layer, (b) buffer layer with 5% of IL, (c) 15% of IL, (d)25% of IL.	34
4.2	Comparison between the obtained films for different deposition parameters. The images, obtained with an optical microscope with 40x magnification, represent: (a) IL 4000 rpm dynamic, (b) IL 2000 rpm dynamic, (c) IL 2000 rpm static.	34
4.3	Colour change of the perovskite layer when the buffer layer is deposited on top of it: (a) no buffer layer (b) 5% of IL (c) 15% of IL.	34
4.4	SEM image in secondary electron mode for the cross section of the reference device and corresponding structure.	35
4.5	SEM images in secondary electron mode and compositional mode for the cross section of the (a),(b) bottom and (c),(d) top devices and corresponding structures.	35
4.7	Reproducibility of the memristor activation over multiple cycles for each configuration: (a) reference,(b) bottom, (c) top.	36

4.6	Reproducibility of the memristor activation in different pixels on the same device and different devices for each configuration: (a) reference,(b) bottom, (c) top with higher current response (d) top with lower current response.	37
4.8	Endurance test over 50 cycles for the top device configuration	37
4.9	I-V response of the (a) reference and (b) top "fresh" devices at 100mV/s and subsequent I-V curves for different scan rates of (c) reference and (d) top devices.	38
4.10	Representation of the choice of V_{read} values in for the (a) reference and (b) top cases and the ON state retention measurement for the (c) reference and (d) top device configuration.	39
4.11	Impedance response for the reference device at 1.2 V.	40
4.12	Capacitance vs frequency at 1.5 V for the (a) reference and (b) bottom devices and at -1.5 V for the (c) top one.	41
4.13	Capacitance as function of the applied voltage for the (a) reference (b) bottom and (c) top configuration.	41
4.14	GIWAXS patterns of different device substrates used as internal marker: (a) FTO, (b) FTO/PEDOT:PSS, and (c) FTO/PEG+IL.	42
4.15	GIWAXS patterns in q-space of the sample FTO/PEDOT:PSS/MAPI for incidence angles α_i (a) smaller and (b) greater than α_c	43
4.16	Integrated intensity profiles for different incidence angles α_i on the FTO/PEDOT:PSS/MAPI sample.	43
4.17	GIWAXS patterns in polar space of the sample FTO/PEDOT:PSS/MAPI for incidence angles α_i (a) smaller and (b) greater than α_c	44
4.18	Azimuthal intensity profiles of the (110) peak for the sample FTO/PEDOT:PSS/MAPI with varying α_i	44
4.19	GIWAXS patterns in q-space of the sample FTO/PEG+IL/MAPI for incidence angles α_i (a) smaller and (b) greater than α_c	45
4.20	Integrated intensity profiles for different incidence angles α_i on the FTO/PEG+IL /MAPI sample.	45
4.21	GIWAXS patterns in polar space of the sample FTO/PEG+IL/MAPI for incidence angles α_i (a) smaller and (b) greater than α_c	46
4.22	Azimuthal intensity profiles of the (110) peak for the sample FTO/PEG+IL/MAPI with varying α_i	46
4.23	GIWAXS patterns in q-space of the sample FTO/PEDOT:PSS/MAPI/PEG+IL for incidence angles α_i (a) smaller and (b) greater than α_c	47
4.24	Integrated intensity profiles for different incidence angles α_i on the FTO/PEDOT:PSS/MAPI/PEG+IL sample.	48
4.25	GIWAXS patterns in polar space of the sample FTO/PEDOT:PSS/MAPI/PEG+IL for incidence angles α_i (a) smaller and (b) greater than α_c	48

4.26 Azimuthal intensity profiles of the (110) peak for the sample FTO/PE-DOT:PSS/MAPI/PEG+IL with varying α_i	49
---	----

Introduction

In the era of rapid technological advancement, optoelectronic devices are going towards their theoretical and physical limits. Simultaneously, the continuous reduction in the size of computing devices, following Moore's Law, where processing power doubles every two years, is approaching fundamental constraints, such as the heat and memory walls. Perovskite emerges as a versatile and promising technology that could potentially address these challenges. The intrinsic hysteretic current-voltage response of perovskite devices allows in-situ data processing where the data is stored, (in-memory computing). In this way, perovskite-based memristor represent a possible alternative to the traditional von Neumann computing architecture, which is approaching its physical limits. In conventional von Neumann computing architectures, the data storage and the processing unit are physically separated leading to high energy consumption in demanding computing tasks. Thus, devices which exhibit intrinsic memory behaviour, the hysteretic I-V, as memristors are considered to be emerging memory concepts for in-memory and neuro-morphic computing. This computational approach seeks to emulate the intricate network of neurons and synapses in the human brain, promising exceptional energy efficiency for data-intensive tasks like big data analysis, machine learning, and artificial intelligence. The theoretical description of memristors, together with the introduction of memristive systems and resistive switching parameters for in-memory computing applications, is presented in Chapter 1. In Chapter 2 perovskites and some of their principal issues are discussed, along with the possibility of using perovskite as material platform for memristive devices, making them suitable for a wide range of applications. The fabrication procedure implemented for the devices studied in this work is described in Chapter 3, where the different techniques used to characterize them are also explained. Finally, in Chapter 4 the main results obtained in the study of three different device configurations are presented. From the characterization of the devices emerged that the introduction of an ionic buffer layer can lead to a deep modification of both the device functionality and perovskite structure. Additionally, the modification is observed to be dependent on the position of the buffer layer in the device configuration.

Chapter 1

Memristors

A memristor is a two-terminal device that undergoes a voltage-controlled conductance change. These memristive devices can be fabricated from various materials, such as silicon oxides, silicon nitrides, metal oxides, and halide perovskites. They may replace, in specific tasks, the transistor, a hallmark of our present-day microelectronics. They are particularly interesting for memory-related applications and, when combined in complex circuits, can perform logic and non-traditional computing operations. The operations take place on the same physical platform where storing occurs, meaning that they can be exploited for non-traditional computing application. This represents an important research direction with the aim of addressing the "von Neumann bottleneck" that affects current computer architectures [1]

It is possible to illustrate the natural emergence of memristive characteristics when a system is exposed to an external field. To achieve this, it can be used the Kubo's response theory. Kubo developed both classical and quantum responses using perturbation theory and although he originally dealt with higher-order perturbations, for simplicity, only the linear response regime is considered here. However, the results and conclusions remain valid in the non-linear case.

The initial step involves calculation of the electrical current density, $\vec{j}(\mathbf{r}, t)$, for a given material subjected to an external electric field, $\vec{E}(\mathbf{r}, t)$. At the microscopic level, it is assumed the knowledge of the many-body electron Hamiltonian, $H(R_E)$, as a function of atomic positions, R_E , for all ions in the material, treated classically, following classical Newton's equations:

$$\frac{d^2 \vec{R}_i}{dt^2} = \frac{\vec{F}(\vec{R}, \frac{d\vec{R}}{dt})}{M} \quad (1.1)$$

Here, M represents ion mass, and F_E is the total force acting on that specific ion. It can be noticed that the force F_E explicitly depends on ion velocity. The dependence is due to electron-ion and ion-ion interactions, which introduce a 'drag' on ions moving in the lattice under an external field. Consequently, the Hamiltonian parametrically depends on ion position and velocity, which themselves obey equations of motion.

At this stage, the electric field perturbation is introduced at time t_0 . To derive the current-current response function, the Kubo's response theory is applied and the following expression is obtained:

$$j_\mu(\mathbf{r}, t) = \int d\mathbf{r}' \int_{t_0}^t dt' \times \sigma \left(\mathbf{r}, \mathbf{r}'; t, t'; \vec{R}, \frac{d\vec{R}}{dt} \right) E_\nu(\mathbf{r}', t') \quad (1.2)$$

This result holds for both quantum and classical treatment of the electron problem. The sum extends over the three spatial coordinates, and $\sigma_{\mu\nu}(\mathbf{r}, \mathbf{r}'; t, t'; \vec{R}, \frac{d\vec{R}}{dt})$ is a 2-rank tensor representing the response. It corresponds to the electrical conductivity of the system in direction μ under the influence of an electric field component in direction ν . This response exhibits spatial non-locality and, fundamental for our purpose, temporal non-locality. This means that conductivity depends on the entire history of the system since the perturbation was introduced. It is crucial to emphasize that this memory is not restricted to electronic degrees of freedom at fixed ionic positions but also originates from ion dynamics and the resulting changes in many-electron configurations, which, in turn, affect the current.

The next step is to consider the electric potential V (assuming the magnetic field induced by the varying electric field is negligible) and write $\vec{E} = -\vec{\nabla}V$. Assuming that the varying electric field induces a negligible magnetic field, we can express, with V as the electric potential, the total current as $I = \int_S \vec{j}$ where $d\vec{S}$ is the infinitesimal surface vector of surface S through which the current is measured. Using equation (1.2), we find :

$$I(t) = G \left(\vec{R}, \frac{d\vec{R}}{dt}, t \right) V(t) \quad (1.3)$$

where the conductance $G \left(\vec{R}, \frac{d\vec{R}}{dt}, t \right)$ for a two-terminal device along the x-direction is given by:

$$G \left(\vec{R}, \frac{d\vec{R}}{dt}, t \right) = - \int_{C_1} d\mathbf{r} \int_{C_2} d\mathbf{r}' \int_{t_0}^t dt' x \sigma(\mathbf{r}, \mathbf{r}'; t, t'; \vec{R}, \frac{d\vec{R}}{dt}) E_\nu(\mathbf{r}', t') \quad (1.4)$$

where the integrals are taken over the far-left and far-right device surfaces C_1 and C_2 . Now, if we define $x_1 = R_E$ and $x_2 = \frac{dR_E}{dt}$, the set of equations from Newton's equation (1.1) yields:

$$I(t) = G(x_1, x_2, t) V(t) \quad (1.5)$$

$$\frac{dx}{dt} = f(x_1, x_2, t) \quad (1.6)$$

defining a memristive system, with x_1 and x_2 being the set of internal state variables (in this particular case, the positions and velocities of all ions in the material).

Eq. 1.5 and 1.6 can be rewritten as:

$$I(t) = C_m \frac{du}{dt} + \frac{1}{R_I} f(u) + x \quad (1.7)$$

$$\tau_k \frac{dx}{dt} = g(x, u) \quad (1.8)$$

where variable $I(t)$ is the current that passes through an inductance L and generates a voltage u_L opposing the increase in current.

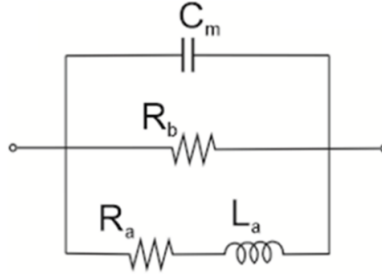


Figure 1.1: Equivalent circuit describing the chemical inductor.

From eq 1.7, three components of the current $I(t)$ can be distinguished: a capacitive charge with capacitance C_m ; a conduction channel characterized by the conductivity function $f(u)$; and a resistance scale parameter R_I . Additionally, eq. 1.8 describes a slow recovery current governed by a voltage-driven adaptation function $g(x, u)$. The first two components in eq 1.7 are considered "fast," because the time constant $\tau_u = R_I C_m$ is significantly shorter than the time constant of the adaptation current, denoted as τ_k . The three separate current branches are associated to three terms of linear impedance :the capacitive and conductive channels, and the RL branch which originate from the delay in eq 1.8. This means that eqs 1.7 and 1.8, for whatever $g(x, u)$, generate a so called chemical inductor whose equivalent circuit is illustrated in Figure 1.1. Three circuit elements are defined as:

$$R_b = \frac{R_I}{f_u}; R_a = -\frac{g_x}{g_u}; L_a = \frac{t_k}{g_u}. \quad (1.9)$$

Depending on the signs of the partial derivatives, positive or negative circuit elements can appear. The effective capacitance of the inductor is:

$$C_L(\omega) = -\frac{1}{L_a \omega^2} \quad (1.10)$$

from which it follows that the inductive element determines a negative value of $\text{Re}(C)$ at a low frequency. This phenomenon is normally referred to as "negative capacitance effect". [2] [3]

1.1 Types of memristive systems

The notion of memory can be defined as the capacity to store the state of a system at a specific moment and subsequently retrieve that information at a later time. This history-dependent alteration of state is a characteristic exhibited by emerging memory devices when subjected to time-varying perturbations, particularly in terms of resistance in memristive systems. A memristive device, which operates based on the history of applied stimuli, is typically a two-terminal structure. Memristive devices are characterized by the presence of a hysteresis loop in the current-voltage (I - V) response, as depicted in Figure 1.2. This memory response can take two forms: "self-crossing", associated with nonvolatile memory, and "not self-crossing", linked to volatile memory.

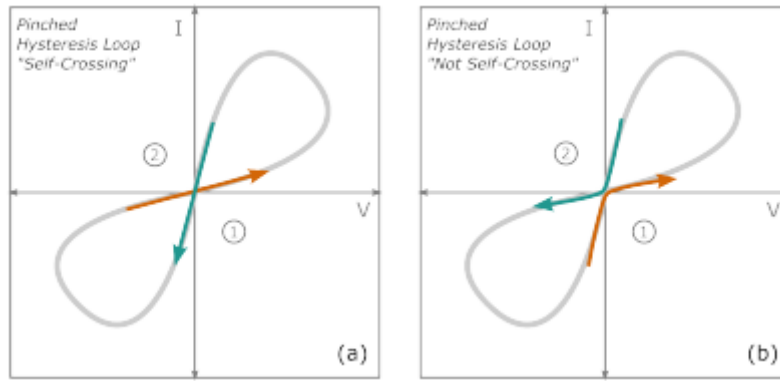


Figure 1.2: Illustration of the hysteresis loop of memristive devices when subjected to periodic stimulus, for both (a) "self-crossing" and (b) "not self-crossing" cases. [4]

The nonlinear dynamic response of memristive systems can be described using the already described equations 1.7 and 1.8. These systems are known as voltage-controlled memristive systems. The response of the current, $I(t)$, is not only dependent on the voltage across the device but also relies on one or more relevant internal state variables, determining the system's state at any given time. Moreover, the transition of the system's state in response to stimuli is not instantaneous but rather influenced by past dynamics. Regardless of the underlying physical mechanisms governing memristive systems, there are changes in the system's conductivity that appear under certain low-frequency periodic stimuli and make the device behave as a nonlinear resistor. The memristive response is denoted as resistive switching. It can be described as the reversible process of two-terminal components that modify their resistance in response to electrical stimuli. Each device configuration can be characterized by a different physical mechanisms causing the resistive switching. In particular, the types of memristive response is determined by the physics of the active material used in the device. The two-electrode technologies which are considered the most attractive and promising are the resistive random access memory

(ReRAM), the phase change memory (PCM), the ferroelectric random access memory (FeRAM), and the spin-transfer torque magnetic random access memory (STT-MRAM). These types of device are illustrated in Figure 1.3, along with the corresponding switching response. [2] [8]

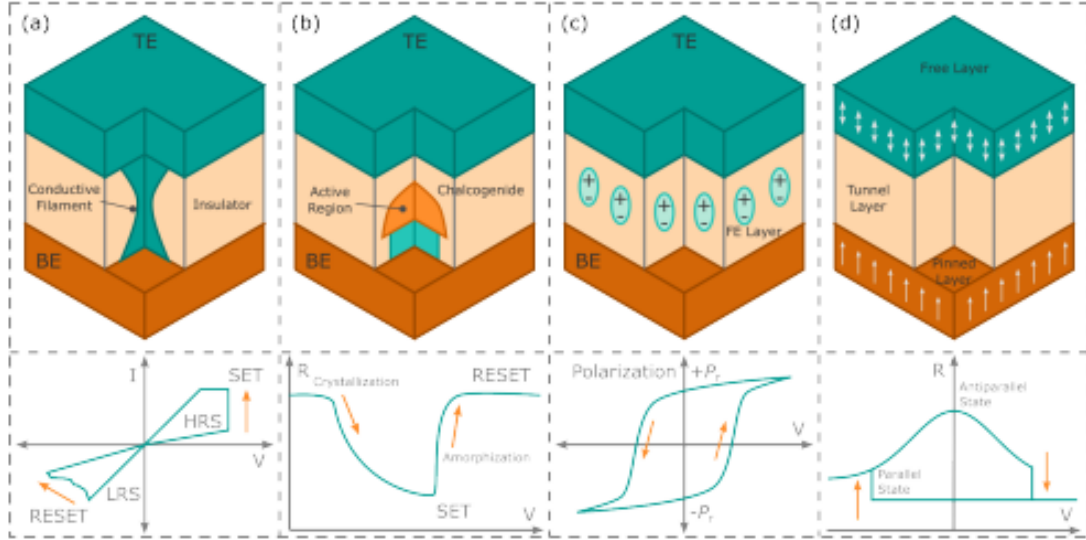


Figure 1.3: Illustration of the two-terminal emerging memory technologies:(a) resistive random access memory (ReRAM), (b) phase change memory (PCM), (c) ferroelectric random access memory (FeRAM), and (d) spin-transfer torque magnetic random access memory (STT-MRAM). [4]

1.1.1 Resistive Switching in ReRAM

The ReRAM consists of a metal-insulator-metal (MIM) configuration with the insulating layer acting as the switching material. The bottom electrode (BE) is typically composed of relatively inert metal, such as Pt or TiN, while the top electrode (TE) is composed of a more reactive metal, such as Ti and Ta. For ReRAMs the resistive switching mechanism consists in the formation of conductive filaments (CF) in the switching material when a voltage is applied. This makes the device switch from a high resistance state (HRS), called OFF state, to a low resistance state (LRS), called ON state. The transition is reversible under the application of a specific external voltage. In devices with gradual resistive switching the possibility of nonfilamentary resistive switching has also been demonstrated. Within ReRAM technology, great efforts have been dedicated to the study and understanding of memristors, with the promise of exceptional memory capabilities tailored for in-memory computing while consuming significantly less energy. The classification of memristor device resistive switching depends on the hysteresis observed

in the current-voltage (I - V) response. This characteristic response is important for determining the relevant performance parameters of these devices. The two principal types of resistive switching mechanisms are the bipolar resistive switching and the threshold resistive switching, described in Figure 1.4.

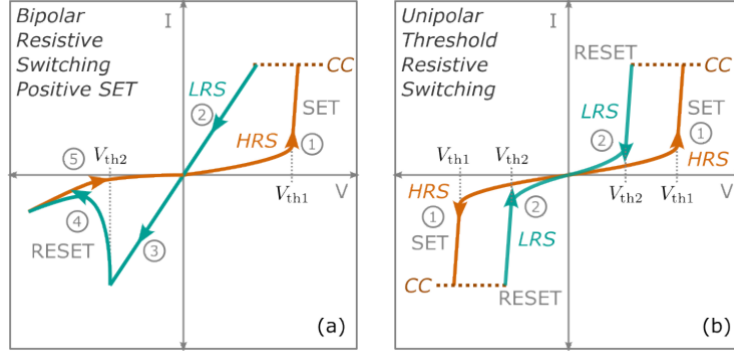


Figure 1.4: Representation of different I - V responses in ReRAM: (a) bipolar resistive switching and (b) threshold resistive switching. [4]

Bipolar Resistive Switching

In the bipolar resistive switching (BRS) the SET process (HRS to LRS) takes place at a specific threshold voltage V_{th1} and the RESET process occurs at a threshold voltage V_{th2} of opposite polarity. BRS-type memristor devices can exhibit either a positive SET with a negative RESET or a negative SET with a positive RESET. In order to avoid irreversible switching that could damage the device during operation, a compliance current (CC) is typically imposed during the SET process. The CC, along with the range for the voltage measurements, is carefully chosen to be sure that the resistive switching is reversible and reproducible. BRS-type devices are characterized by nonvolatile memory, where the ON state current is maintained even when the external voltage is removed. [4]

Threshold Resistive Switching

Differently from the previous case, in threshold resistive switching both the SET and RESET processes take place at the same polarity. The SET process occurs at a threshold voltage V_{th1} while the RESET process take place in the reverse scan direction at a lower threshold voltage V_{th2} , within the same polarity as the SET process. As for BRS, a compliance current (CC) is implemented to prevent the damage of the device. Threshold switching devices have also shown SET and RESET processes in either positive or negative polarities. These devices are characterized by volatile memory, where the ON state goes back to the OFF state when the external voltage is removed or is significantly reduced. [4]

1.2 Characteristics of Memory Devices

The implementation of these emerging devices in memory applications depends on their performance characteristics, in particular, on the storage and logic capabilities. Based on these characteristics, different devices exhibit suitability for a different application in neuromorphic computing paradigms, as for example deep neural networks (DNN) and spiking neural networks (SNN). The characteristics of the memristor devices can be defined as follows [6]:

- **Multilevel operation:** The number of measurable charge or current states. A bit represents two logic states – “0” or “1”.
- **Write voltage:** The external voltage required to set the device state or the “write” process. The writing operation may be called the store operation.
- **Write time:** The time required to effectively promote the write processor to store the information.
- **Read time:** The time required to effectively measure or sense the state of the device, “read” process, at a specific read voltage. The reading process is called "recall operation".
- **Write energy:** The energy needed to store one bit.
- **Linearity:** The linearity of the conductance changes depending on the electrical stimulus.
- **Integration density:** The number of memory devices that could be integrated in a single chip.
- **Retention:** The time passed between the data storage and the first incorrect readout of the data.
- **Endurance:** The minimum number of write-read cycles that the device can endure.

1.3 Comparison of Emerging Memory Technologies

A comprehensive comparison of the performance characteristics of the emerging memory devices can be found in Table 1.1. Notably, both FeRAM and STT-MRAM exhibit exceptional endurance cycles and operate with low write energies. However, their functionalities are limited to single-bit operations, making them particularly suitable for digital computing schemes that incorporate spiking neural networks (SNN). In contrast,

ReRAMs and PCMs offer the possibility of multi-level operations with substantial endurance cycles and efficient write energies. Furthermore, these devices show a nonlinear switching behavior and provide multi-level conductance tuning, making them particularly suitable for implementations in deep neural networks (DNN) and SNN. Nonetheless, it is important to note that due to the temperature-dependent switching characteristics of PCMs, their operational efficiency falls behind other emerging technologies. Consequently, ReRAMs emerge as promising candidates for further studies and development. [6] [7]

Technology	ReRAM	PCM	FeRAM	STT-MRAM
Multilevel operation	multibit	multibit	1 bit	1 bit
Write voltage (V)	<3	<3	<3	<1.5
Write time (ns)	<10	50	30	<10
Read time (ns)	<10	<10	<10	<10
Write energy (J/bit)	0.1 - 1 pJ	~ 10 pJ	~ 100 fJ	~ 100 fJ
Linearity	Low	Low	None	None
Integration density	High	High	Low	High
Retention	Medium	Long	Long	Medium
Endurance	$10^5 - 10^8$	$10^6 - 10^9$	10^{10}	10^{15}
Suitability for DNN training	Low	Low	No	No
Suitability for DNN inference	Moderate	Yes	No	No
Suitability for SNN algorithms	Yes	Yes	Yes	Moderate

Table 1.1: Comparison of different emerging memory technologies. [4]

1.4 Performance parameters of memristors

The performance parameters of memristors are derived from their characteristic current-voltage (I - V) responses. Typically, I - V curves are plotted using a semilog scale, representing $\log|I|$ vs V , which accentuates the key parameters. Figure 1.5 illustrates a schematic representation of a logarithmic $|I|$ - V curve for a bipolar resistive switching (BRS) type ReRAM device.

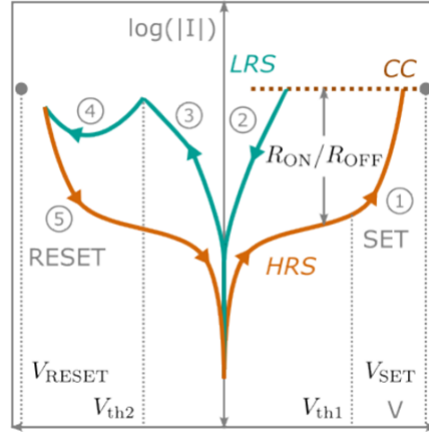


Figure 1.5: Typical I-V curve in semilogarithmic scale for a BRS type ReRAM device and performance parameters. [4]

The definitions of the performance parameters for ReRAM devices are the following:

- **Current states:** The current levels of the High Resistance State (I_{HRS} or I_{OFF}) and Low Resistance State (I_{LRS} or I_{ON}) that are directly identified from the I-V curve.
- **Resistance states:** The resistance values related to the HRS (R_{HRS} or R_{OFF}) and LRS (R_{LRS} or R_{ON}), directly measured or calculated through $R = dV/dI$.
- **ON/OFF ratio:** The ratio between the resistance (R_{ON}/R_{OFF}) or the current (I_{ON}/I_{OFF}) of the ON state and the OFF state.
- **SET voltage V_{SET} :** The voltage that has to be applied to promote the SET process, with $V_{SET} > V_{th1}$.
- **RESET voltage V_{RESET} :** The voltage that has to be applied to promote the RESET process, with $V_{RESET} < V_{th2}$ for BRS and threshold RS.
- **Endurance:** The number of switching cycles the device can endure until the ON/OFF becomes indistinguishable.
- **Switching speed:** The minimum duration of an externally applied voltage pulse at V_{SET} required to induce the SET process from HRS to LRS
- **Retention time:** How long the ON or OFF state is maintained without applying an external voltage following the SET or RESET process, respectively.
- **Operation energy per bit:** The energy necessary to promote the SET process of the ReRAM, it is calculated through $E = qV = qIR$.

- **Scalability:** The geometrical dimension at which a ReRAM device can be scaled down before reaching intrinsic physical limits.
- **Two-state storage / binary switching:** ReRAM characterized by two separate states – the HRS, OFF state assigned to logic “0” state, and the LRS, ON state assigned to logic “1” state.
- **Multilevel or multistate storage / analog switching:** The ReRAM’s ability to achieve different resistance or current states upon the applied V_{SET} , V_{RESET} or current compliance (CC).
- **Threshold switching:** ReRAM characterized by a threshold resistive switching where the ON state relaxes to the OFF state when the the applied external voltage is removed or sufficiently decreased.

Chapter 2

Hybrid perovskites

The term “perovskite” is used to describe a class of materials having the same crystal structure as calcium titanate (CaTiO_3), a mineral discovered in Ural mountains of Russia by Gustav Rose in 1839 and named after Russian mineralogist Lev Perovski. In general, perovskites are compounds with a crystal structure of ABX_3 , where A is a monovalent cation, B is a divalent cation, and X is a halide anion. [9] [10].

Over the past decade, hybrid halide perovskites have garnered significant attention as promising semiconductors for optoelectronic devices. Combining both organic and inorganic characteristics, these perovskites consist of a halide X anion and an organic A cation. Their distinctive physical properties, such as a high absorption coefficient, long-range charge transport, and an adjustable energy gap, make them highly attractive and cost-effective materials for photovoltaic applications. This has resulted in a remarkable increase in the efficiency of solar cell power conversion. Since perovskites are a class of materials, it becomes straightforward to imagine the range of properties that various types of these compounds can exhibit.

Among the different types, hybrid metal halide perovskites, specifically those where B represents the metallic element, have garnered significant attention due to their favorable energy band gap for photovoltaic applications. The principal example is methylammonium lead iodide (MAPbI_3), widely employed as active layer in solar cells, featuring an energy gap of 1.55 eV. Another important example is methylammonium lead bromide (MAPbBr_3), unsuitable for photovoltaic applications due to its excessively high energy band gap of 2.3 eV. However, it proves to be an excellent candidate for radiation detection, owing to its considerable mobility, extended carrier lifetime, and the high atomic numbers of Pb and Br. In the following, the principal characteristics of perovskites and their application in memristor devices will be presented, with a focus on MAPbI_3 .

2.1 Crystal structure

In the perovskite structure of cubic ABX_3 , an A-site cation is enclosed within a cage structure constituted by B-site cations and X-site anions. The B atom is sixfold coordinated with X atoms, creating a BX_6 octahedron interconnected at all corners, resulting in a three-dimensional perovskite network, as illustrated in Figure 2.1. Specifically, hybrid halide perovskites consist of a monovalent organic A-site cation ($CH_3NH_3^+$ or $HC(NH_3)_2^+$), divalent B-site group IV cations (Pb_2^+ , Sn_2^+ , and Ge_2^+), and X-site halide anions (Br^- , I^- , Cl^-), maintaining charge neutrality as $A^+B_2^+(X^-)_3$. In methylammonium lead iodide, the Pb_2^+ cation is positioned at $(\frac{1}{2}, \frac{1}{2}, \frac{1}{2})$ and coordinates with 6 neighbouring iodide ions, forming corner-sharing $[PbI_6]^{4-}$ octahedra. The organic cation MA^+ is positioned at the center $(0, 0, 0)$, surrounded by eight $[PbI_6]^{4-}$ octahedra and twelve iodide ions (I^-), located at $(\frac{1}{2}, \frac{1}{2}, 0)$, $(\frac{1}{2}, 0, \frac{1}{2})$, and $(0, \frac{1}{2}, \frac{1}{2})$. The special structure of BX_6 octahedra mostly contributes to the peculiar optoelectrical properties of perovskite. [11] [12]

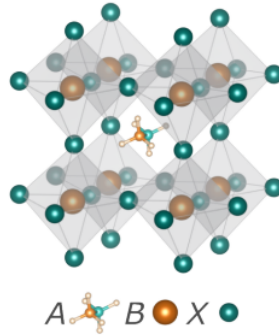


Figure 2.1: Crystal structure of a cubic ABX_3 perovskite. [4]

Depending on the temperature, $MAPbI_3$ exhibits different crystal symmetries, summarized in Table 2.1 with the corresponding space groups and lattice constants. The most common non-cubic perovskite structures are the tetragonal and orthorhombic phases. They are characterized by a three-dimensional network of corner-sharing octahedra. In the tetragonal phase there is just one nonzero tilting angle, while in the orthorhombic phase all the tilting angles are different from zero. At room temperature $MAPbI_3$ assume a tetragonal structure (space group $p4/mcm$). Increasing the temperature, at $T=327.4$ K there is the transition to the cubic phase ($Pm3m$), accompanied by a slight distortion of the PbI_6 octahedra. The orthorhombic symmetry (with space group $Pna2_1$) is achieved when the temperature goes below 162.2 K. [14] In order to predict in which structure the perovskite would arrange, the so called Goldschmidt tolerance factor (t) is used. It is a relevant structural parameter for expressing the stability of perovskite compounds. It is a dimensionless value defined as

	T(K)	Christalline phase	Space group	Lattice constant (Å)
α -MAPbI ₃	>327.4	cubic	Pm3m	a= 632.85
β -MAPbI ₃	162.2-327.4	tetragonal	I4/mcm	a= 885.5 c = 1265.9
γ -MAPbI ₃	< 162.2	orthorhombic	Pna2 ₁	a= 886.1 b= 858.1 c = 1262.0

Table 2.1: Temperature dependent structural data of MAPbI₃

$$t = \frac{r_A + r_X}{\sqrt{2}(r_B + r_X)}$$

where r_A , r_B , and r_X are the ionic radii of the A, B, and X atoms. To understand the meaning of t , let us consider a unit cell as illustrated in Figure 2.2, in which at the center there is the B-site cation such that there are alternating atomic planes formed of A-X and B-X atoms. Looking at the scheme, it is easy to understand that the tolerance factor represents the ratio of the diagonal distances in the alternating planes. In fact, the diagonal distance from the center of the square to corner is $r_A + r_X$ for the A-X plane and $\sqrt{2}(r_B + r_X)$ for the B-X plane .

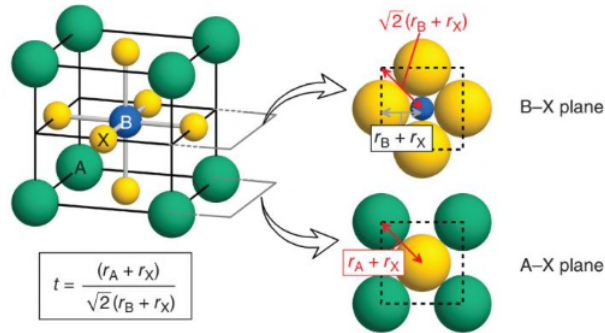


Figure 2.2: Representation of the Goldschmidt's tolerance factor a perovskite structure, where r_A , r_B , and r_X are the ionic radii of the A-, B-, and X-site atoms. [13]

To calculate t , knowing the actual values of r_A , r_B , and r_X is important, but in general the calculation of ionic radii is difficult. In fact, ions are not rigid spheres and the peripheral conditions have an impact on their size, causing the calculation of an accurate t value to be a challenging task. Ideally, $t > 1$ determine hexagonal or tetragonal structures, $1 > t > 0.9$ results in a cubic structure, $0.9 > t > 0.71$ produces an orthorhombic or rhombohedral structure, while $t < 0.71$ does not determine a perovskite

crystal structure. In general, materials with tolerance factor ranging between 0.81 and 1.01 are considered to have a perovskite structure. [27] [17]

2.1.1 Hysteresis and ionic transport

Ionic transport has been identified as one of the main factors contributing to the intrinsic hysteretic effects characterizing the electrical response of perovskites. In perovskite solar cells (PSCs), hysteresis occurs in scan direction–dependent $J-V$ curves. They are generally classified into normal and inverted hysteresis as illustrated in Figure 2.3. The device exhibits normal hysteresis when the current levels are higher in the reverse scan compared to the forward scan direction. However, devices with different formulations can show higher current levels in the forward scan than the reverse scan.

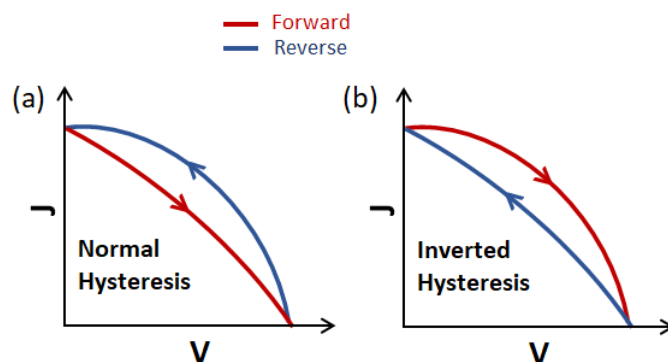


Figure 2.3: Scan direction dependence for the (a) normal-type hysteresis and (b) inverted-type hysteresis.

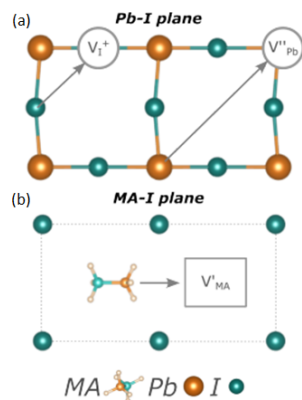


Figure 2.4: Scheme of three ionic transport mechanisms in MAPbI_3 due to (a) I^- , Pb^{2+} and (b) MA^+ migration. [4]

Considering MAPbI₃, under the application of an external electric field, three ionic transport mechanisms have been identified: iodide migration along an octaedron edge, Pb²⁺ migration along the diagonal $\langle 110 \rangle$ direction of the cubic unit cell, and MA⁺ migration into a neighboring vacant A-site (Figure 2.4). The migration of the iodide vacancy (V_I^+) shows an activation energy lower than the one related to MA⁺ vacancy (V_{MA}^+) and Pb²⁺ vacancy (V_{Pb}^{2+}), indicating that MAPbI₃ is a mixed ionic-electronic conductors where the I⁻ ions represent the majority ionic carriers. [16] The vacancies migration under the influence of an external electric field could determine a change in the photogenerated charge collection efficiency with time, leading to the hysteresis in JV measurements. Moreover, metal ions and dopants have also been reported to migrate into the perovskite layer contributing to the hysteresis, detrimental for example for solar cells stability but which represents the possibility of using this materials for memory application.

2.2 Stability issues

Perovskites are affected by instability mainly due to the intrinsic ion migration, but there are also some external factors due to the environment as moisture, oxygen, light, and heat. Water is one of the main factors that affects perovskite materials, causing irreversible degradation leading to the transformation of perovskite into its precursors. In particular, in the case of MAPbI₃, water facilitates the creation of hydrate complexes, such as (CH₃NH₃)₄PbI₆ · 2H₂O, determining the PbI₂ crystallization. During the hydration process, both monohydrate and dihydrate phases can develop, following the reactions, respectively:



An important consequence of the hydration process of perovskite is the structural alteration of the (PbI_6)⁴⁻ octahedra. The 3D network becomes a 1D chain for the monohydrate and a 0D configuration for dihydrates. The structural deformation affects the chemical bonds between the A-site component and (PbI_6)⁴⁻, determining the weakening of the bonds and increasing the susceptibility of the material to other harmful factors such as heat and electric bias. When the moisture saturates the perovskite, the process becomes irreversible, eventually resulting in the production of CH₃NH₃I and PbI₂. A representation of the moisture effect on perovskite films is reported in Figure 2.5

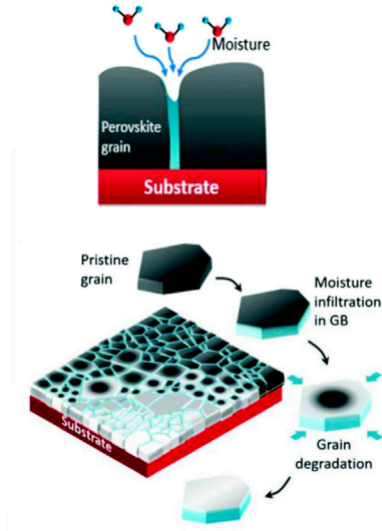
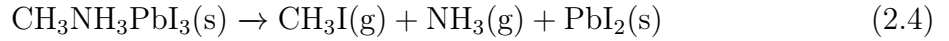


Figure 2.5: Representation of the degradation mechanism induced by moisture in perovskite film. [17]

Temperature constitutes another important factor influencing perovskite stability. In MAPbI_3 case, the exposure to a temperature of 85°C , in inert atmosphere conditions, leads to the following detrimental reactions [17] [18]:



Additionally, photo-oxidation has also an impact on the stability of metal halide perovskites, leading to a detrimental effect for the material when exposed to oxygen and light. Figure 2.6 shows the schematic of the photo-oxidation process in MAPbI_3 that can lead to the material breakdown. The process can be divided in three steps. In the first one, O_2^- is formed due to photo-excited electrons interacting with the O_2 close to the surface of MAPbI_3 . During the second step, O_2^- reacts with $(\text{CH}_3\text{NH}_3)^+$ and Pb , leading to the formation of H_2O and $\text{Pb}(\text{OH})_2$ on the MAI-terminated surface and the $\text{Pb}-\text{I}$ bond breaks because of Pb oxidation on the PbI_2^- terminated surface. In the third step, following the production of water molecules in surface oxidation, a hydration process develop in the inner perovskite. [19]

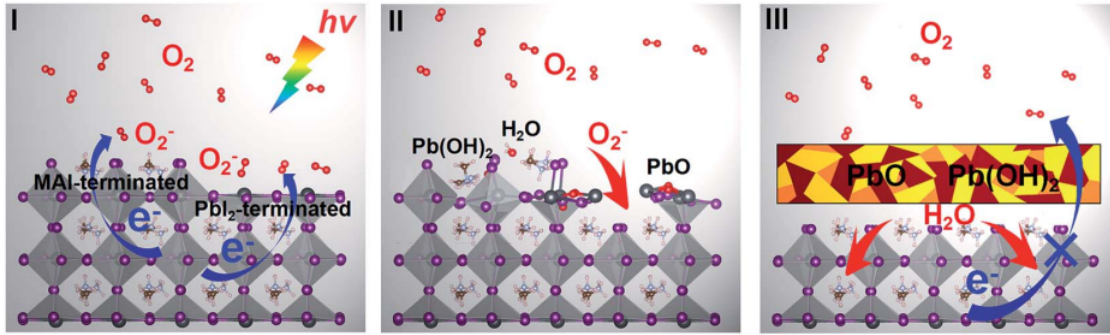


Figure 2.6: Representation of the three steps photo-oxidative process determining degradation in MAPbI₃ (001) surface. [19]

2.3 Perovskites in Memristor Technology

Thanks to their ionic-electronic conductivity, perovskites have gained particular attention as switching materials in resistive random-access memory (ReRAM) devices for neuromorphic computing applications. In the context of solar cells, the memristive response in perovskites exhibits an inverted hysteresis under dark conditions, a phenomenon previously reported in the literature for PSCs. The extensive research and understanding of PSCs for photovoltaic applications can be exploited for the integration of perovskites as switching materials in memristor technology .

These materials offer a versatile platform for memristive devices, with switching physics suitable for a wide range of neuromorphic computing architectures [24]. The possibility of playing with perovskite formulations increases the internal state variables in the devices. Moreover, the choice of the top and bottom electrodes plays a crucial role in determining the switching type and performance of the device [118–120]. The choice of electrochemically reactive (e.g., Ag, Al, Cu, Ti) or non-reactive (e.g., Pt, Au) top electrodes, as well as the symmetry or asymmetry of the bottom electrode (BE) with respect to the top electrode (TE), introduces additional design flexibility. Another variable is the possibility to incorporate intermediate buffer layers at the interface between the perovskite switching layer and the electrodes for various purposes, such as protection (e.g., PMMA), capping, or carrier transport (e.g., PCBM, PEDOT:PSS, Spiro-OMeTAD). [4] [20]

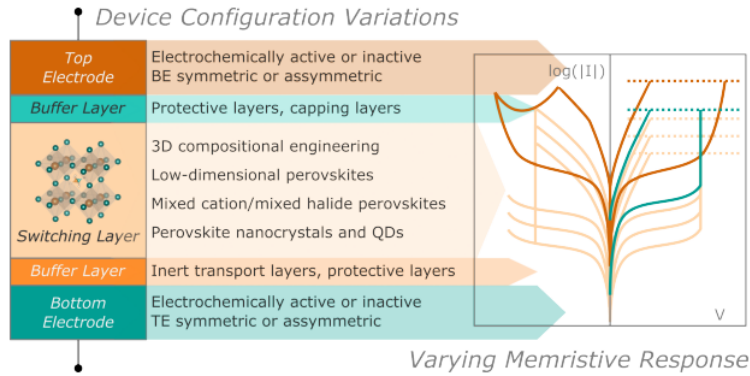


Figure 2.7: Scheme of a perovskite-based memristors and different device configurations influencing the memristive response. [4]

A wide range of device configurations has demonstrated outstanding properties for in-memory applications. State-of-the-art perovskite memristors with non-volatile bipolar switching exhibit impressive ON/OFF ratios ranging from $\sim 10^2$ to 10^9 , retention times exceeding 10^3 seconds, and endurance exceeding 10^3 cycles. Furthermore, memristors with volatile threshold switching mechanism have shown multi-state memory capabilities suitable for analog applications, exhibiting multiple synaptic functions for neuromorphic computing.

2.3.1 Switching mechanism

The switching mechanism behind the memristor activation is not completely clear yet. In general, the switching mechanisms in perovskite memristors can be classified into nonfilamentary switching, and filamentary switching (Figure 2.8). Applying an external voltage V_{SET} , induces a specific switching mechanism tailored to the device configuration, allowing the transition from HRS to a LRS. Depending on the resistive switching type, the application of a specific V_{RESET} switch off the device from the LRS to the HRS. V_{RESET} needs to be opposite in polarity for bipolar switching devices and lower in voltage in the same polarity for threshold switching devices.

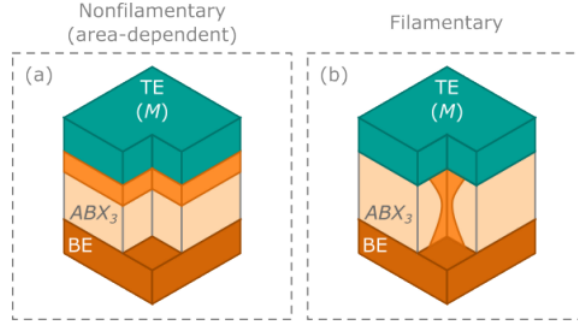


Figure 2.8: Scheme of ABX_3 perovskite based memristors with (a) nonfilamentary switching, and (b) filamentary switching mechanisms. [4]

Nonfilamentary switching is determined by the change in the device conductivity when an external field is applied. This modification is caused by ionic migration and redistribution or interfacial reactivity of the migrating ion species with the top metal electrode. The mobile X^- ions and V_X^+ defects in the perovskite are uniformly distributed when the device is in the initial state, called "FRESH" state. When the voltage V_{SET} is applied, the motion of the ions and defects to the top and bottom electrodes, respectively, is activated. The accumulation of ions and defects at the interfaces between perovskite and contacts leads to the change in the overall conductance of the device. The case of filamentary switching is characterized by the formation of conductive filaments (CF) in the perovskite due to the application of an external field, destroyed during the RESET process. The CF can be constituted of halide vacancies V_X^+ or activated metal ions (M^+). In the first case the filament is said to form through valence change mechanism while in the second one through electrochemical metallization. The ions and vacancies, from the FRESH state, move towards their corresponding electrodes and accumulate at the interface between perovskite and electrode. A further diffusion of the V_X^+ -rich towards the BE is determined by the continuous application of the external field, leading to the formation of a vacancy conductive filament connecting the two electrodes.

However, even if the memristive response for perovskite based devices has been studied for a large amount of configurations, a complete picture of the underlying switching mechanism is still missing. [21] [22]

2.3.2 Application

The memristive response of ReRAMs (section 1.1) allows in-situ computation characterized by the storage of data in the same place. The co-location of the data processing and storage allows the miniaturization of the effective device sizes. This results in high density network structures mimicking the characteristic processes of neurons and synapses in

the human brain, with the aim to achieve significant energy efficiency. The ReRAMs can be exploited as artificially intelligent hardware for big data analysis, machine learning, and neuromorphic computing (for "in-memory computation" in general). The implementation in different in-memory computing frameworks depends on the particular switching type and performance parameters of ReRAMs. Perovskite represent a versatile choice as switching material. The architectures for in-memory computation are based on the ionic-electronic conductivity of perovskites but also their optical properties can be exploited. Thus, they can be used as synaptic hardware but also to generate photocurrent, allowing application of perovskite-based memristor as photosynaptic tools for artificial visual perception systems, neuromuscular systems, pupil reflex, and applications in light-sensitive optogenetics. In general, the specific memristive response of the device determine the possible applications. In order to tailor the device design for specific and more complex computational applications, the understanding of the underlying mechanisms in the kinetics of ionic motion and the possibility to manipulate the switching mechanism of these devices are fundamental aspects. The control of the ON/OFF ratio, one of the main device parameters, is not an easy task since it is calculated as the difference between the HRS and the LRS upon switching. In the HRS, before the switching takes place, the current levels depend on the conductivity of the device configuration that is influenced by factors as the perovskite formulation, incorporation of buffer layers, dopants, nanocrystals, and also the individual layer thicknesses. [23] [24]

Chapter 3

Methods

3.1 Device fabrication

One of the factors that contribute to the hysteresis in perovskite-based device is the ionic migration. For this reason, in order to study how the hysteretic response of memristors can be manipulated, it is added to the system a certain amount of iodide ions (I^-). Methylammonium lead iodide ($MAPbI_3$) is used as active layer for the memristor the so it is expected that the additional iodide can take the place of vacancy and contribute to the transport in the perovskite. The introduction of ions is performed by using an ionic liquid embedded in a supporting matrix. For this purpose it was chosen the poly(ethylene glycol), because it is already used as polymeric matrix in lithium batteries. [25]

In this work, three different configurations for the memristor are tested

- FTO/PEDOT:PSS/ $MAPbI_3$ /Au (reference)
- FTO/PEDOT:PSS/ $MAPbI_3$ /PEG+IL/Au (top)
- FTO/PEG+IL/ $MAPbI_3$ /Au (bottom)

The reference configuration has been chosen because its behaviour has been already studied, while the top and bottom configurations and are new.

The step-by-step fabrication method is schematically illustrated in Fig.3.2 while the three complete devices are represented in Fig.3.1

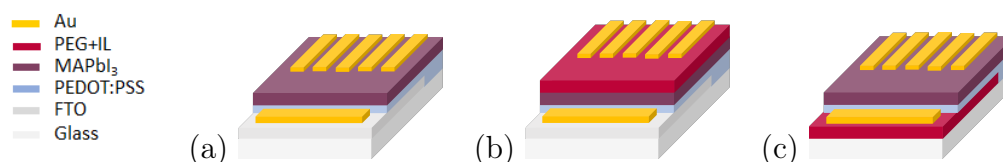


Figure 3.1: Device configurations tested in this work:(a) no buffer layer (reference), (b) buffer layer on top of MAPI layer(top), (c) buffer layer below of MAPI layer (bottom).

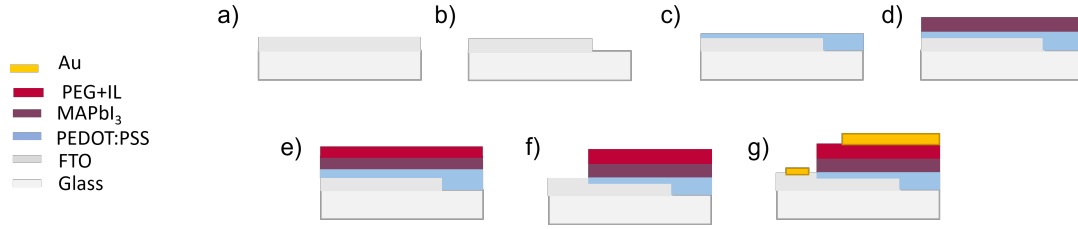


Figure 3.2: cross section of the device in the "top" configuration at each step of the fabrication:(a) substrate (b) etched FTO, (c) pedot, (d) MAPI, (e) PEG+IL, (f) scratched substrate, (g)gold contacts

Substrate selection

Highly transparent fluorine doped tin oxide (FTO) on TEC15 glass substrates ($2.5 \times 2.5 \text{ cm}^2$) are used as the transparent bottom electrode. The FTO-coated glass substrates are carefully selected to have highly uniform, unscratched, and homogeneous surface required for the deposition of high-quality thin films.

FTO etching and cleaning

The FTO-coated glass substrates are partially etched using zinc (Zn) powder and a 2M hydrochloric (HCl) solution. Each of the etched substrates is brushed with Extran detergent solution in order to remove any residues of the etching process, then brushed under water and rinsed. The brushed samples are subjected to a sequence of 5 minutes sonication in deionized water with Extran followed by sonication in acetone, and isopropyl alcohol. Finally, the cleaned samples are blow-dried using a nitrogen gun.

PEDOT:PSS deposition

A poly(3,4-ethylenedioxythiophene) polystyrene sulfonate (PEDOT:PSS) layer is deposited on top of the FTO-coated glass substrate with the function of allowing a better deposition of the perovskite and a better wettability. In order to remove residual organic contamination on the surface and improve the surface wetting, the cleaned substrates are subjected to an ultraviolet-ozone (UV-O₃) treatment for 15 minutes prior to the deposition of the PEDOT:PSS layer. The deposition of the PEDOT:PSS solution (Clevios P VP.Al 4083, Heraeus) is carried out in ambient conditions, after letting the solution reach room temperature. The PEDOT:PSS solution is dropped, using a syringe, onto the etched FTO substrate until the whole surface is covered (8-10 drops), while filtering it using a PTFE (hydrophilic) $0.45 \mu\text{m}$ filter. The substrate is then spin coated with PEDOT:PSS filtered solution for 30 s at 3000 RPM with a 1000 RPM/s acceleration.

At the end of the spin-coating process, the samples are annealed at 100°C for 5 minutes and then are immediately placed inside the nitrogen-controlled glove box.

Perovskite preparation and deposition

A MAPbI₃ precursor solution is prepared dissolving 681.5 mg lead iodide (PbI₂) (>98, TCI) in 95 μ L dimethylsulfoxide (DMSO) (\geq 99.9, Sigma Aldrich) and 1 mL N,N-dimethylformamide (DMF) (99.8, Sigma Aldrich) solution. After waiting at least two hours the PbI₂ is completely dissolved, the PbI₂ precursor solution is added to 235 mg methylammonium iodide (MAI) (>99.9, Greatcell Solar) to complete the 1.4 M MAPbI₃ precursor solution. a 50 μ L MAPbI₃ perovskite solution is statically spin coated onto the PEDOT:PSS layer for 50 s at 4000 RPM with 1000 RPM/s acceleration. After 8 s from the start of spin coating sequence, a 500 μ L chlorobenzene (CB) anti-solvent is dynamically injected onto the MAPbI₃ solution to promote the crystallization of high quality and homogeneous perovskite films. Once the spin coating sequence ends, the samples are annealed at 100 °C for 10 mins.

Buffer layer solution preparation and deposition

For the preparation of the buffer layer a solution of 20 mg/L of poly(ethylene glycol) 20000* (PEG) in isopropyl alcohol (anhydrous,99.5%) is prepared. In order to obtain the solution, it is heated at 65°C, and it is maintained at the same temperature while using because it solidifies when it starts to cool down (Fig.3.3).

For what concern the ionic liquid, since the viscosity of the liquid make difficult to measure the volume, the 1-butyl-3-methylimidazolium idide (IL) and isopropyl alcohol (IPA) are separately weighted and then mixed, in order to obtain a 10% solution in weight of IL in IPA. The two solutions are filtered with an hydrophobic 0.45 μ m filter and then mixed to obtain the desired percentage of IL solution in PEG solution (doped PEG). Prior to the deposition, the substrates are heated at 65 °C for 5 minutes in order to delay the solidification of the solution before the complete deposition. 200 μ L of doped PEG solution is deposited via dynamic spin coating with 2000 rpm and an acceleration of 1000 rpm/s for 30 s. The solution is dropped within the first 4s of the procedure

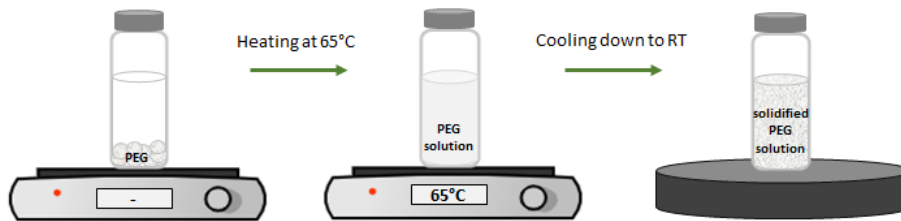


Figure 3.3: PEG solution preparation in IPA.

Metal contact deposition

The deposition of the top Au metal contacts is realized through resistive thermal evaporation, using a commercial Oerlikon Leybold Univex 250 evaporation chamber. A three-step sequence of evaporation rates is used to obtain a homogeneous 85 nm Au layer: (i) 0.05 Å/s from 0 – 1 nm, (ii) 0.5 Å/s from 1 – 10 nm, and (iii) 1.0 Å/s from 10 – 85 nm.

PMMA protective layer

In order to protect the device from the moisture exposition, a poly(methyl methacrylate) (PMMA) layer can be deposited on top of the complete device. 60 μL of as 25 mg/L solution of PMMA in toluene is spin-coated onto the device at 2000 rpm for 30 s with an acceleration of 1000 rpm/s. [26]

1x1 cm² device

Following the same procedure previously illustrated, a version of the three devices with 1x1 cm² dimension has been fabricated. The lack of a specific mask for the evaporation of contact on a smaller substrate has required the modification of the contacts geometry, as schematized in Fig.3.4.

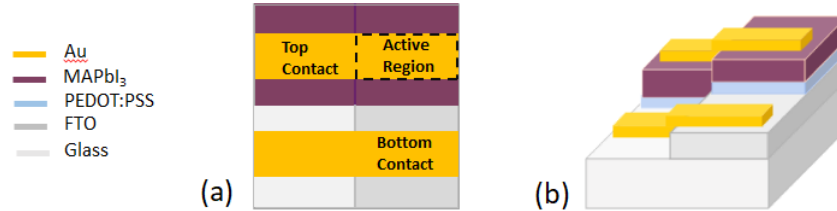


Figure 3.4: (a) Top view and (b) cross section of the 1x1 cm² memristor configuration

3.2 Device characterization

3.2.1 Cyclic voltammetry and retention measurements

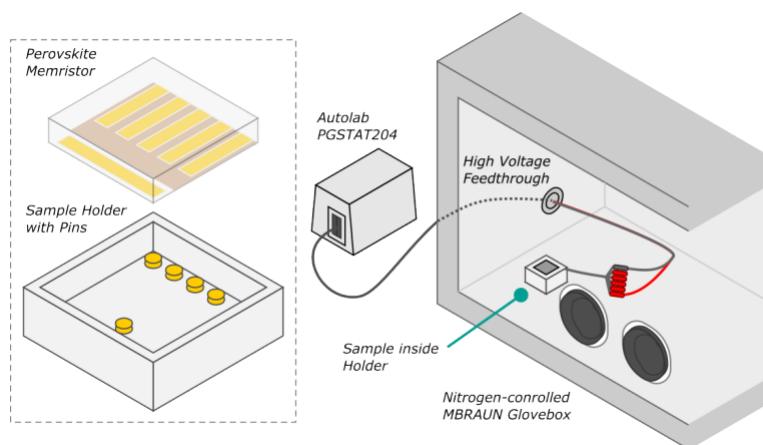


Figure 3.5: Schematic diagram of the characteristic I V response and chronoamperometry measurement of memristors inside the nitrogen-filled glove box.

In order to electrically characterize the memristors, the characteristic I-V response are measured via cyclic voltammetry (CV) method under dark condition inside a nitrogen-filled MBRAUN M200 glove box using an Autolab PGSTAT204 potentiostat, as schematically illustrated in Fig. 3.5. The response is measured by varying the voltage range and performing multiple cycles. The starting and ending voltages of the procedure are always 0V, the upper voltage and the lower one are decided depending on the device configuration, but in any case they are chosen to be equal and opposite in sign so to obtain a symmetric range. The sequence of measurement for the devices started at 0.8V for the reference configuration, 1V for the top configuration, and 0.5V for the bottom one, the voltage limit is increased gradually in order to avoid an abrupt increase of the current that above 10 mA could lead to the damaging of the device. The maximum applied voltage is chosen in such a way to not overcome this current value.

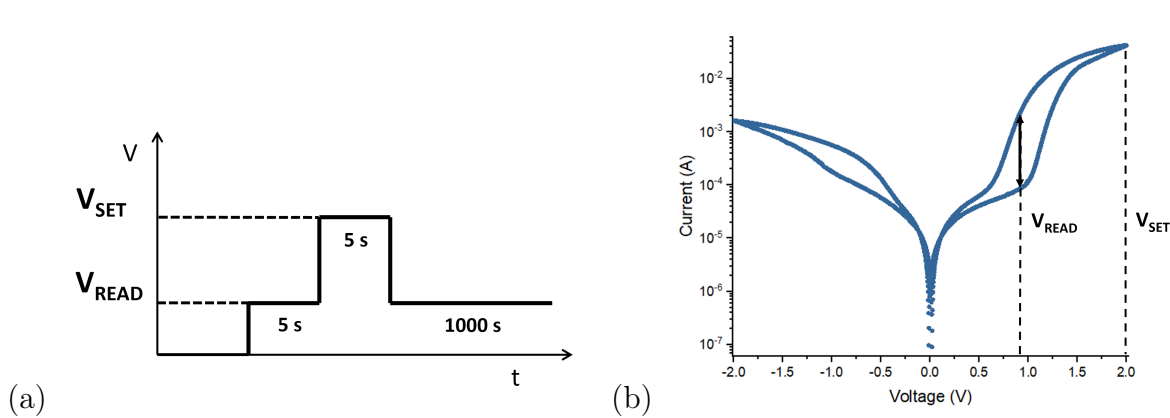


Figure 3.6: (a) Series of voltages applied to the device, (b) definition of V_{READ} and V_{SET} .

The dynamic transition state was investigated via chronoamperometry, following the procedure illustrated in Fig.3.6. A series of voltages V_{READ} , V_{SET} for 5s each one and V_{READ} again for 1000s. It is applied to the device. V_{READ} is defined as the voltage for which the ON/OFF ratio is maximum, while V_{SET} is defined as a voltage at which the device is active (Fig3.6.b). This allows to study the device's retention capability of the ON state.

3.2.2 Impedance Spectroscopy

When a voltage is applied to a perovskite-based device, an ionic accumulation occurs at the interface of the contacts, resulting in a noticeable variation of the capacitance. To get insights into the ionic accumulation phenomenon in the new memristor's configuration, a series of impedance measurements have been performed. [28]. The impedance measurements were conducted using both a Keysight E4980A LCR meter and with an Autolab PGSTAT204. In Fig. 3.7 a sketch of the sample used to perform the measurements is shown. The memristor is mounted on a mica substrate, a thermoconductive and electrically insulating material, with two copper pads connected to the device's gold contacts using gold wires and silver paste. The measurements were performed with the sample placed in a Nextron microprobestation under vacuum conditions, as illustrated in Fig. 3.7b.

For both instruments the impedance measurements are based on the same principles. Impedance spectroscopy involves the application of a small perturbation of an oscillating voltage $\tilde{V}(\omega) = V_m \sin(\omega t)$ at a frequency $f = (\omega)/2\pi$ in addition to a DC voltage, and the resulting steady state current $\tilde{I}(\omega) = I_m \sin(\omega t)\theta(\omega)$ is measured. Here, V_m is the amplitude of perturbation, I_m is the amplitude of the steady-state current, and θ is the phase of $\tilde{I}(\omega)$ relative to $\tilde{V}(\omega)$. The impedance is then calculated by $Z(\omega) = \frac{\tilde{V}(\omega)}{\tilde{I}(\omega)}$. It

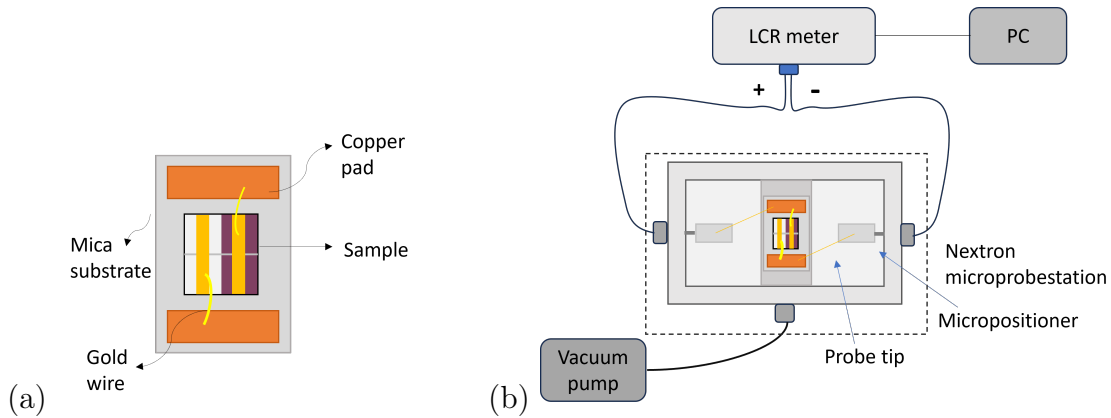


Figure 3.7: Schematic representation of the sample mounted on a mica substrate with copper contacts(a) and the experimental setup(b) for the impedance measurements using both the keysight LCR meter and the Autolab PGSTAT204.

can also be expressed in complex form as $xccZ(\omega) = Z'(\omega) + iZ''(\omega)$ and the impedances related to the ideal circuit elements are $Z_R(\omega) = R$, $Z_C(\omega) = \frac{1}{i\omega C}$ and $Z_L(\omega) = i\omega L$.

The main difference between the two types of impedance measurements performed is that in the LCR meter it is necessary to select an equivalent circuit from a list of proposed ones, and the output provides R, C, or L as function of the bias voltage or the perturbation frequency, which is limited at 20 Hz. On the contrary, with the Autolab the output is given by Z, Z' and Z'' as function of the frequency and it is necessary to implement appropriate equivalent circuit models to extract the circuit parameter values. Since the effect of ionic contact phenomena can be observed at low frequency, the measurements with the LCR meter were performed at a working frequency of 50 Hz, value close to the instrument limit, varying the applied DC voltage, ranging between 0V and 1.4V in step of 100 mV. The circuit in Fig. 3.8b is the one chosen for the measurements, in fact a memristor can be described with the equivalent circuit illustrated in Fig. ?? and for voltages in which the device is in low conduction state, the circuit can be approximated to a parallel between a resistance and a capacitance and when the threshold voltage for transition to the high conduction state has been reached it is expected a negative capacitance that can correspond to an inductive behaviour.

For what concern the measurement performed with the Autolab, the impedance spectra of the devices were acquired in a frequency range spanning between 100kHz and 0.1Hz, for different DC voltages, and the circuit parameters need to be extracted with further analysis. [31] [32]

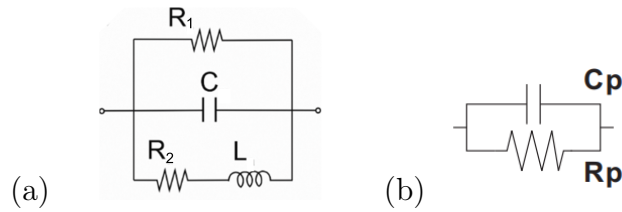


Figure 3.8: (a) Equivalent circuit representative of a memristor and (b) equivalent circuit chosen to perform the impedance measurements with the LCR meter.

3.2.3 Scanning Electron Microscope

A Field Emission Scanning Electron Microscope (FE–SEM) with a JSM-700F JEOL FEG-SEM system operating at 15 keV was used to obtain images of the three devices through secondary (SEI) and backscattered (COMPO) electron detection. Secondary electrons are used to observe the topography of the specimen surface, while backscattered electrons are mainly used to observe the compositional differences of the specimen.

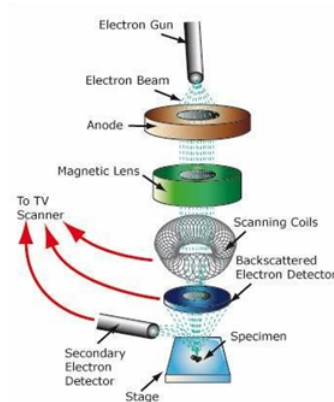


Figure 3.9: Scheme of a scanning electron microscope.

The high-energy electrons beam is emitted from a field-emission electron gun, accelerated and then focused using a series of electromagnetic lenses, under vacuum conditions. The beam can run across the sample surface in a systematic manner, line by line, to scan the entire region of interest. When the beam strikes the sample surface, it interacts with the atoms in the material in different ways. One of the most common interactions is the inelastic scattering of electrons, known as secondary electron emission. In this process, the high-energy primary electrons transfer some of their energy to the outermost electrons (valence electrons) of the sample atoms, causing them to be ejected from the surface with an energy lower than the primary electron's one. As the primary electron

beam is scanned across the sample, the detector records the intensity of secondary electrons emitted from different points on the surface. The collected data is then used to construct a grayscale image, where brighter areas correspond to regions emitting more secondary electrons, and darker areas correspond to regions emitting fewer secondary electrons. showing the surface topography of the sample The image reveals features such as surface roughness, morphology, and other surface details.

Another type of electron-sample interaction in the SEM is elastic scattering, specifically backscattering of electrons. When the high-energy electrons strike the sample, some of them undergo backscattering, bouncing back with higher energy and are recorded with solid state detectors, placed above the sample. The number of backscattered electrons and their energy depend on the atomic number of the sample's elements (the higher the atomic number, the larger the emission volume), and they originate from deeper areas of the sample than the secondary electrons. If the sample surface has differences in composition, backscattered electron emission will acquire the compositional contrast determined by the average atomic number of a component. Regions with higher average atomic number elements (more backscattered electrons) appear brighter in the backscattered electron image, while lower atomic number regions (fewer backscattered electrons) appear darker. Thus, backscattered electron imaging allows to estimate the location of high atomic number materials on the sample, offer insights into the sample's elemental composition and density variations.

The dependence of the intensity of backscattered electron on the atomic number is not linear and it results that small differences in mean atomic nuclei are easier to detect at lower atomic numbers. Moreover, backscattered electrons are highly directional; they are emitted in the direction of specular reflection with reference to the incident angle on the sample surface. As a result, backscattered electron emission can detect subtle topographical differences that cannot be identified in secondary electron imaging. [27]

3.2.4 Grazing Incidence Wide Angle X-ray Scattering

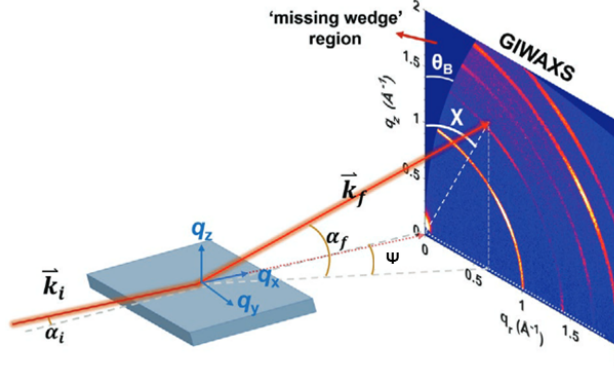


Figure 3.10: Sketch of the GIWAXS experiment geometry.

The memristors have been characterized with Grazing Incidence Wide Angle X-ray Scattering (GIWAXS) measurements performed at the XRD1 beamline of Elettra Synchrotron. GIWAXS is a technique used to study the structure and ordering of crystalline materials, such as thin films, nanomaterials, and surfaces, with high sensitivity to molecular arrangements and crystallographic orientations. This technique is particularly valuable for investigating materials with preferential orientation or nanostructures that are difficult to analyze using conventional X-ray diffraction (XRD) techniques.

The geometry used for GIWAXS experiments is illustrated in Fig 3.10, the coordinate system used is represented onto the sample surface at the point of diffraction, with the z-axis in the normal direction and the x and y ones parallel to the sample surface. The collimation of X-ray beam (200 μm in size) is achieved through specialized mirrors or slits, which ensure that the incident X-rays are well-defined and focused onto the sample surface. In the beam path it is placed a beam stop with the function of blocking the direct beam and the spill over of intense diffuse scattering in the scattering plane. The set up include also a shutter that is synchronized with the measurement and blocks irradiation of the sample between data collection to limit potential beam damage. Since the geometrical alignment of the sample is fundamental, the sample holder is connected to a precise motor positioning system and it is essential that the surface of the sample is centered on the rotation point of the three spatial tilts, otherwise it can occur a relative translation of the beam with respect to a given tilt direction. The scattered X-ray photons are recorded using a specialized pixelated area detector, with CMOS hybrid-pixel technology operating in single-photon-counting mode, which converts the X-ray photons directly into electric signals and creates a 2D map of the reciprocal space. The data are collected over a certain range of incident angles and visualized on the screen as debye-scherrer rings, as represented in Fig. 3.10. This pattern contains structural

information and is used to extract data about the crystallographic orientation, lattice parameters, and nanostructural features of the material

In 3D, the scattering wavevector is given by

$$\vec{q} = \begin{pmatrix} q_x \\ q_y \\ q_z \end{pmatrix} = \begin{pmatrix} \cos\alpha_f \cos\Psi - \cos\alpha_i \\ \cos\alpha_i \sin\Psi \\ \sin\alpha_i + \sin\alpha_f \end{pmatrix}$$

The information it is possible to get is that in case of randomly oriented planes the signal leads to an homogenous intensity dis-tributions in the Debye–Scherrer rings, while the directional scattering due to highly-oriented scattering planes leads to non-uniform distributions.

The scattering vector is directly influenced by the wavenumber k_0 , which is determined by factors such as the wavelength of the monochromatic X-rays (λ), the incident angle (α_i), and the exiting angles (α_f, Ψ) of the scattered X-rays. As a consequence, the choice of X-ray energy affect the scattering angles. Increasing or decreasing the X-ray energy determines a reduction or enlarging of the exiting angles for a given crystallographic scattering plane. An higher energy allows to map a larger area of reciprocal space, but it hinders the resolving power of the detector, composed of pixels with defined sizes. In fact, considering as fixed the sample geometry and the distance between sample and detector, the total reciprocal space that can be recorded depends on the active area of the detector and it is inversely dependent to the sample-to-detector distance. On the other hand, the angular resolution is inversely related to the pixel size but directly dependent on the distance between the sample and the detector. Thus, it is necessary to find a trade off between measuring a large range in reciprocal space and obtaining an high angular resolution. [30]

Chapter 4

Results and Discussion

4.1 Introduction of the buffer layer

The procedure for the preparation and the deposition of the ionic buffer layer, described in section 3.1, has been established after trying different conditions. As first step, the percentage of IL in the solution needed to be decided. To do so, different concentrations were tested and it was observed the worsening of the wettability of the PEG+IL solution when the amount of IL in the system increases, as it can be noticed in Figure 4.1. Nevertheless, the presence of PEG, an insulating material, reduces the current that the device can reach for a certain applied voltage, so it is important to have as much IL as possible, maintaining the homogeneity of the film. Taking into account the insulation caused by PEG and the necessity of having an homogeneous film, 15% was considered the most suitable amount of IL.

In order to decide the deposition parameters, different conditions were tested and the resulting films are shown in Figure 4.2. The first set of parameters tested was the one used for the deposition of the PEDOT:PSS layer, described in section 3.1, but injecting the solution once the spin-coater is on (dynamic). The film was compared with the one obtained using 2000 rpm instead of 4000 rpm and it was chosen the lower velocity.

The possibility of injecting the solution while the spin-coater is still off (static) was also tested, but the dynamic option was considered the best one in order to avoid the cooling and solidification of the solution before the substrate has been completely covered.

Once the conditions for obtaining an high-quality homogeneous layer were found, the PEG+IL layer was deposited on top of the MAPI one (FTO/MAPI/PEG+IL) considering both the case with 5% and 15% of IL concentration to see if there are changes in the perovskite colour, indicating an interaction between the perovskite layer and the PEG+IL one. In Figure 4.3 a change in the perovskite colour could be noticed when the buffer layer was added to the system. The difference increases with increasing the amount of IL, which suggests in particular an interaction with the ionic liquid.

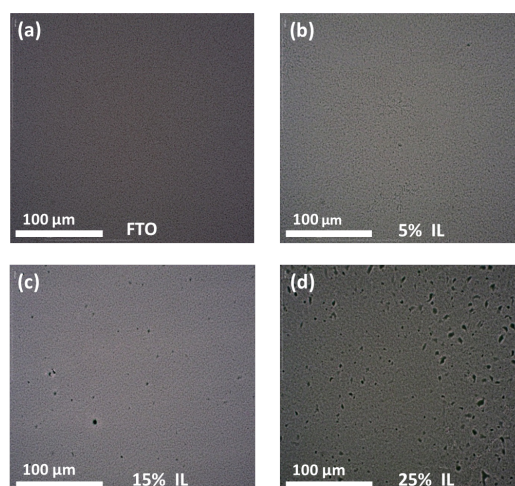


Figure 4.1: Comparison between the obtained films for different concentration of IL. The images, obtained with an optical microscope with 40x magnification, represent: (a) FTO substrate without PEG+IL layer, (b) buffer layer with 5% of IL, (c) 15% of IL, (d) 25% of IL.

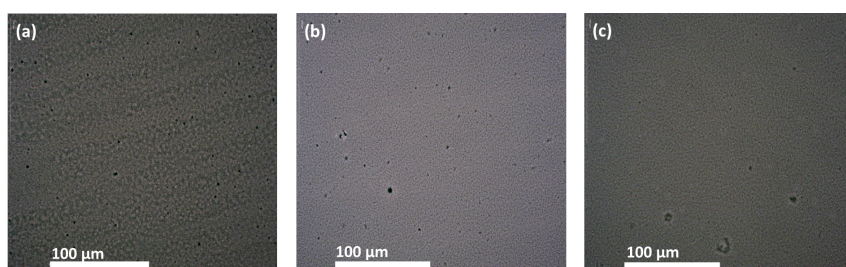


Figure 4.2: Comparison between the obtained films for different deposition parameters. The images, obtained with an optical microscope with 40x magnification, represent: (a) IL 4000 rpm dynamic, (b) IL 2000 rpm dynamic, (c) IL 2000 rpm static.

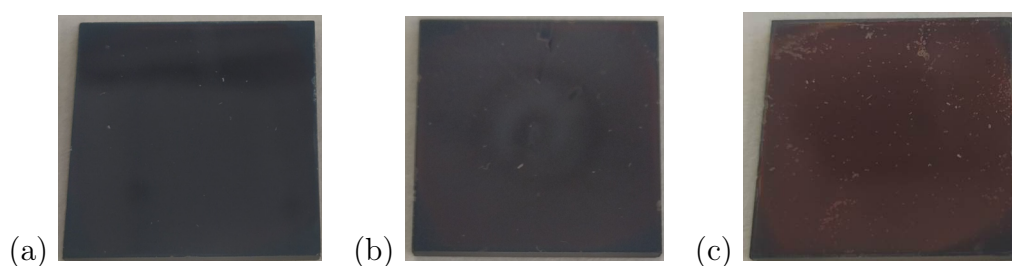


Figure 4.3: Colour change of the perovskite layer when the buffer layer is deposited on top of it: (a) no buffer layer (b) 5% of IL (c) 15% of IL.

Finally, the ionic buffer layer was incorporated in the FTO/PEDOT:PSS/MAPbI₃/Au system in the bottom and top configurations. To assess its impact on the MAPI layer, SEM images in SEI and COMPO mode have been captured in the cross-sectional view. In the bottom configuration (Figure 4.5(a)) a different crystallization of MAPI with respect to the reference (Figure 4.4) can be noticed, while in the SEI image of the top configuration (Figure 4.5(c)), a difference in MAPI thickness compared to the reference is observable. The thickness of the MAPI layer is expected to be almost 400 nm and the thickness of the buffer layer should be 50 nm, but from the SEM image the MAPI and the buffer layer seem to have almost the same thickness, being MAPI thinner than expected, while the buffer layer is thicker than expected. This is more evident in the COMPO image (Figure 4.5(d)) and suggests that what was initially thought to be PEG+IL was likely perovskite modified by the presence of the ionic liquid which can penetrate in MAPI. In particular, iodide ions can penetrate and occupy the iodide vacancies of MAPI.

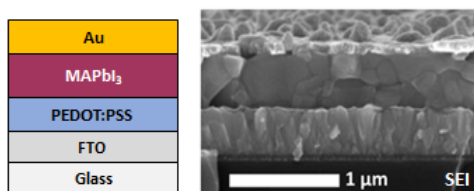


Figure 4.4: SEM image in secondary electron mode for the cross section of the reference device and corresponding structure.

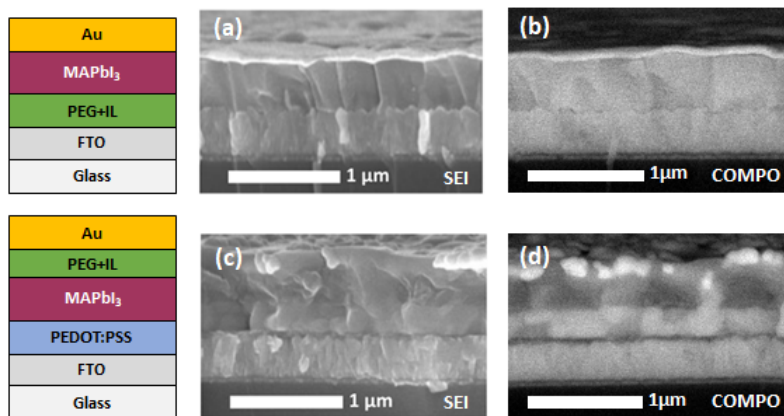


Figure 4.5: SEM images in secondary electron mode and compositional mode for the cross section of the (a),(b) bottom and (c),(d) top devices and corresponding structures.

4.2 Electrical response

The current-voltage (I-V) response of the device allows to see how the hysteresis is affected by the changes in the device configuration.

In Figure 4.6 the I-V response of the three different device configurations are illustrated and it is highlighted the reproducibility of the response for different contacts (pixels) on the same device and for different devices. The obtained reference behaviour is in accordance with the literature's one [33] while the response of the two new configuration indicate a relevant effect due to the presence of the buffer layer. Looking at the I-V curve of the bottom device structure, the device activates for lower voltage than the reference and it can be noticed a larger hysteresis than the reference one. The top configuration shows the most interesting result since the activation of the device appear for negative voltages (Au(-); FTO(+)), a behaviour never observed for the already studied memristor configurations. Moreover, for the top configuration two kind of response have been seen: the devices fabricated before summer show higher currents (from 10^{-7} A to 10^{-2} A) than the devices fabricated during summer (from 10^{-10} A to 10^{-5} A). A reason for this result can be found in the higher temperature and humidity in the laboratory during summer. Since for the scratching and evaporation step the samples stay outside the the glovebox, the room conditions can influence the device response. [34] The reproducibility over multiple cycle (Figure 4.7) was also verified. While in the reference and top case the devices activate and then reset at each cycle, in the bottom case the device does not go back to the initial state after the first cycle and stays active.

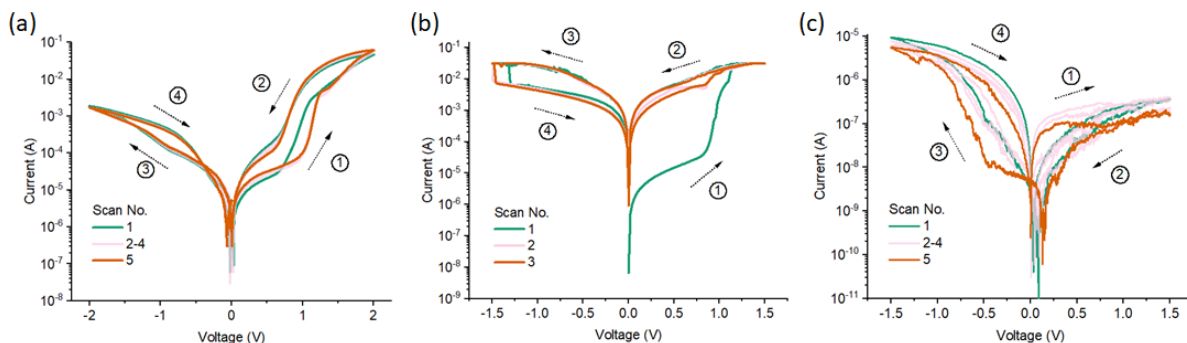


Figure 4.7: Reproducibility of the memristor activation over multiple cycles for each configuration: (a) reference,(b) bottom, (c) top.

For the top configuration an endurance test, in which the device has been cycled for 50 times, was also performed. As it can be seen in figure 4.8, after 50 cycles the device response is still the same.

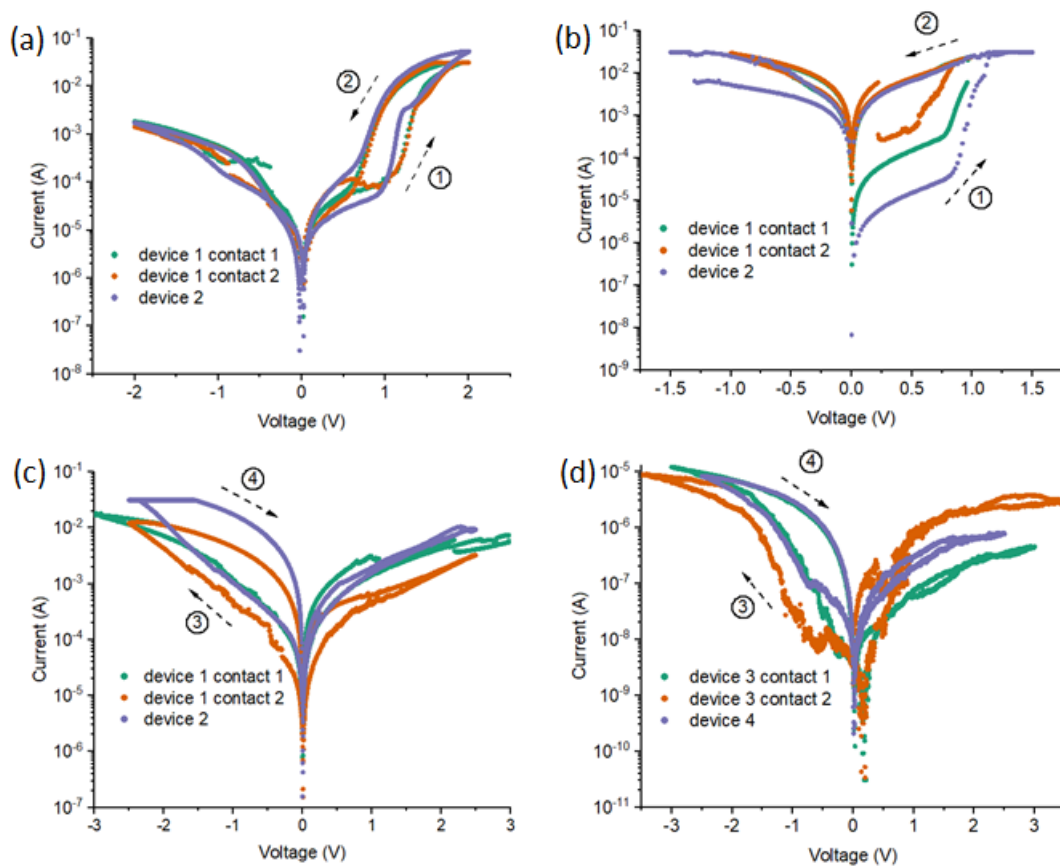


Figure 4.6: Reproducibility of the memristor activation in different pixels on the same device and different devices for each configuration: (a) reference, (b) bottom, (c) top with higher current response (d) top with lower current response.

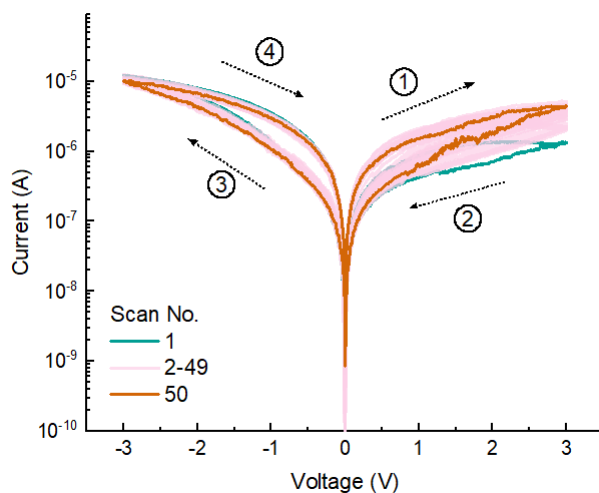


Figure 4.8: Endurance test over 50 cycles for the top device configuration

An explanation for the difference in the polarity activation in the top configuration can be found in the fact that in the new device there is a reservoir of iodide on top of the MAPI region which determines a larger amount of ions moving from the top electrode to the bottom electrode when the negative bias is applied. The opposite happens in the bottom configuration, where the iodide reservoir is between FTO and MAPI. Then, a large hysteresis is present in the first scan due to the large amount of ions which move from the bottom electrode to the top electrode for positive applied voltages. Since the device does not recover the initial OFF state, it is possible that the ions coming from the buffer layer take the place of the iodide vacancies in the perovskite and remain there. In Figure 4.9 I-V measurements performed for scan rate values ranging from 5V/s to 50mV/s are shown. It can be observed that decreasing the scan rate value the current increases in both cases. In the reference the hysteresis is larger for higher scan rate values, meaning that those are the values of the characteristic time scale of ion redistribution, while in the top it is evident a reduction of the hysteresis with respect to the "fresh" device one.

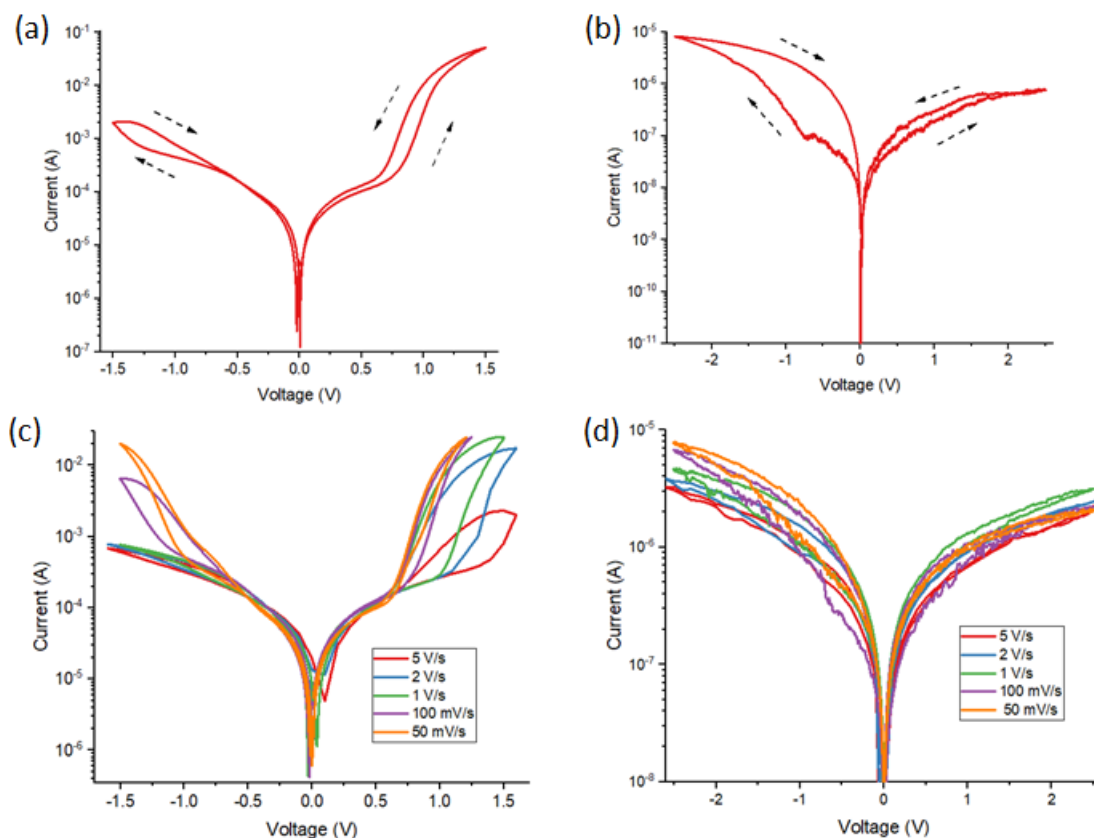


Figure 4.9: I-V response of the (a) reference and (b) top "fresh" devices at 100mV/s and subsequent I-V curves for different scan rates of (c) reference and (d) top devices.

Figure 4.10(c) and 4.10(d) illustrate the capability of the reference and top device configuration to retain the ON state. In the images the current when a voltage V_{read} is applied before (pre pulse) and after (post pulse) the application of V_{SET} is plotted. In both cases the current levels of the pre pulse and post pulse are in agreement with the current levels in the I-V curves in Figure 4.10(a) and 4.10(b). Looking at the post pulse, in both cases there is an initial discharge due to the previous application of V_{SET} . For the reference device, the increasing of the current with time can be noticed. This behaviour is probably due to the fact that the chosen V_{read} value is close to the threshold voltage for the device activation and the continuous application in time of such a voltage can promote the set process. On the contrary, for the top device configuration V_{read} is close to the reset threshold, for this reason it goes back to the OFF state.

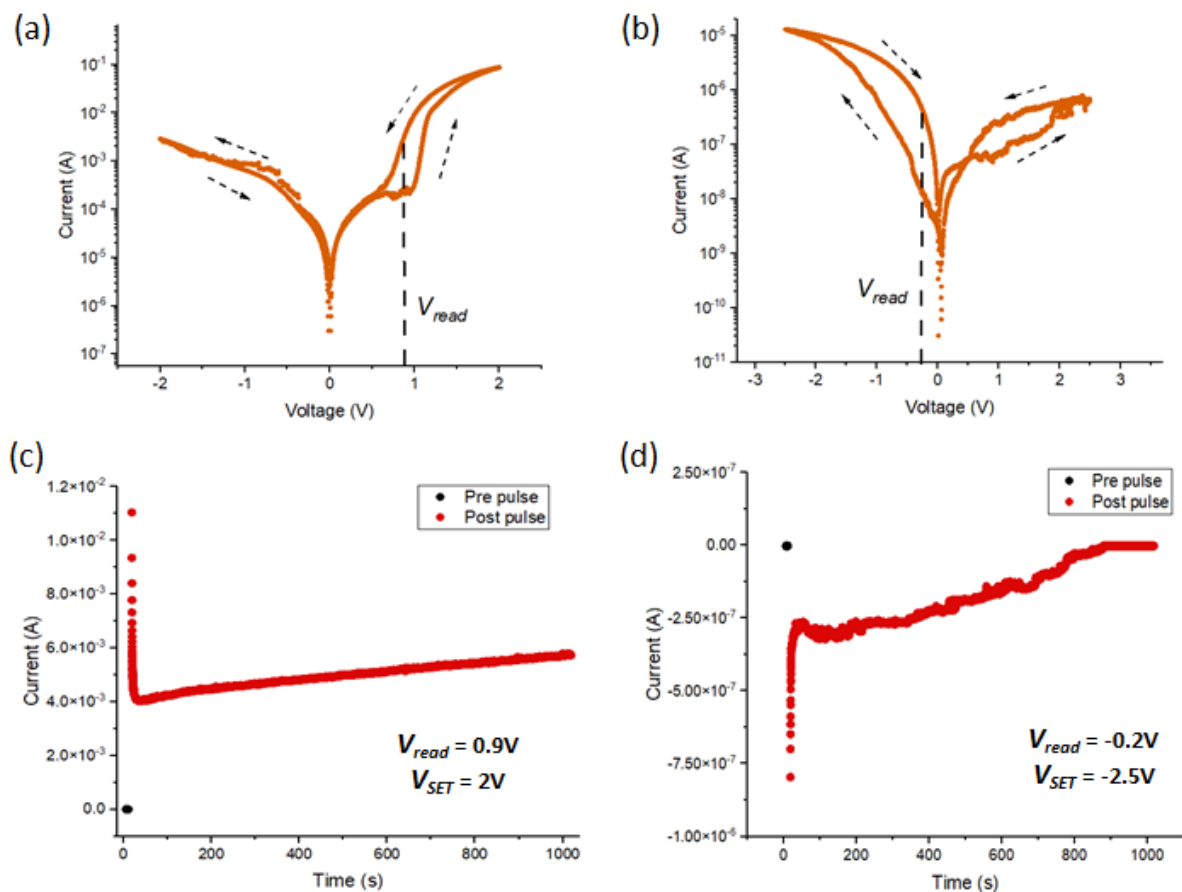


Figure 4.10: Representation of the choice of V_{read} values in for the (a) reference and (b) top cases and the ON state retention measurement for the (c) reference and (d) top device configuration.

4.3 Impedance Spectroscopy

The impedance measurements for the three devices were performed with the objective of getting insight into the ionic transport in the material, responsible for the electrical response. Unfortunately, the obtained data were very noisy, as shown in Figure 4.11. Due to the noise it was not possible to extract valuable information from these measurements.

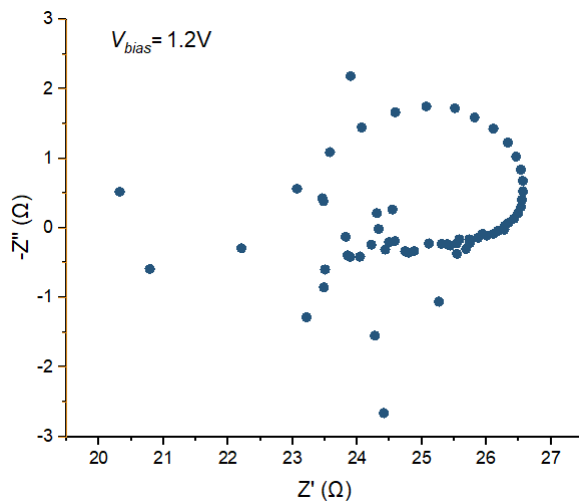


Figure 4.11: Impedance response for the reference device at 1.2 V.

A different kind of impedance measurements were performed through a keysight LCR meter. With this measurements it was possible to check the expected capacitive behaviour of the samples, described through the chemical inductor model illustrated in Chapter 1.

Looking at the absolute value of the capacitance measurements as function of the frequency (Figure 4.12), an inflection point can be noticed when the capacitance value became negative for low frequency ($\sim 10^2$ Hz). This is in agreement with the literature, where the negative capacitance and inductive features are reported to appear at low frequency, where the ionic transport, determining the hysteretic behaviour, gain importance. [3]

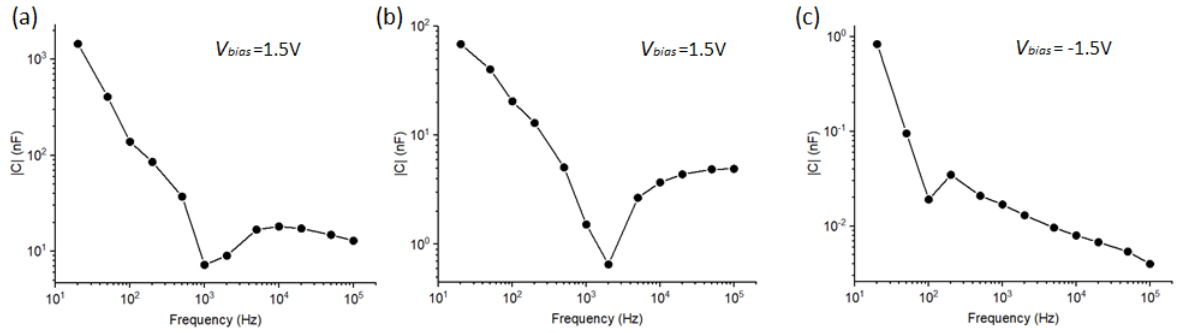


Figure 4.12: Capacitance vs frequency at 1.5 V for the (a) reference and (b) bottom devices and at -1.5 V for the (c) top one.

In Figure 4.13 the capacitance as function of the voltage applied to the device is shown. In each of the three cases the capacitance became negative when the device activates (for $V > 0$ in the reference and bottom case and for $V < 0$ for the top case). Additionally, by substituting the capacitor in the circuit with an inductor, it was verified that the appearance of the negative capacitance corresponds to a positive inductance.

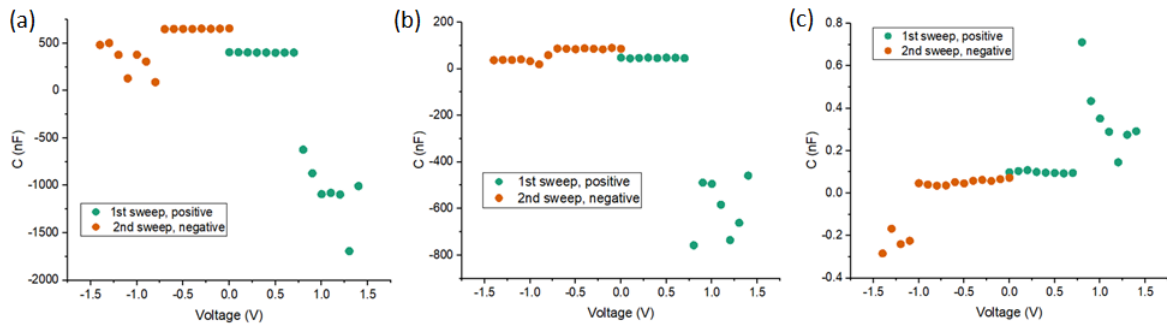


Figure 4.13: Capacitance as function of the applied voltage for the (a) reference (b) bottom and (c) top configuration.

4.4 Grazing Incidence Wide Angles X-ray Scattering

In GIWAXS measurements, especially in the case of multiple layers samples, the calculation of the critical angle α_c of the material is fundamental. In fact, based on this value, it is possible to determine if the signal observed for a certain incident angle α_i is coming from the surface ($\alpha_i < \alpha_c$) or from the whole structure ($\alpha_i > \alpha_c$). This angle can be calculated as $\alpha_c \sim \sqrt{2\delta}$ where δ is the refractive index decrement which can be determined with a specific calculator once the density ρ is known [35]. The ρ and α_c values for the materials constituting the devices under study are reported in Table 4.1. For a multiple layer structure, the considered critical angle is the one referred to the upper layer. Since

	PEDOT:PSS	PEG+IL	MAPI
ρ	1 g/cm ³	1.12 g/cm ³	4.12 g/cm ³
α_c	0.10 °	0.10 °	0.17°

Table 4.1: Density ρ and critical angle α_c of the different layers in the devices.

a memristor is composed by multiple layers, it is important to understand which signal is characteristic of a specific material. To do so, the substrates composed by FTO/PEDOT:PSS, FTO/PEG+IL, and FTO alone were used as reference signals, representing an internal marker to know when the whole device is observed. The GIWAXS patterns observed for these samples are shown in Figure 4.14.

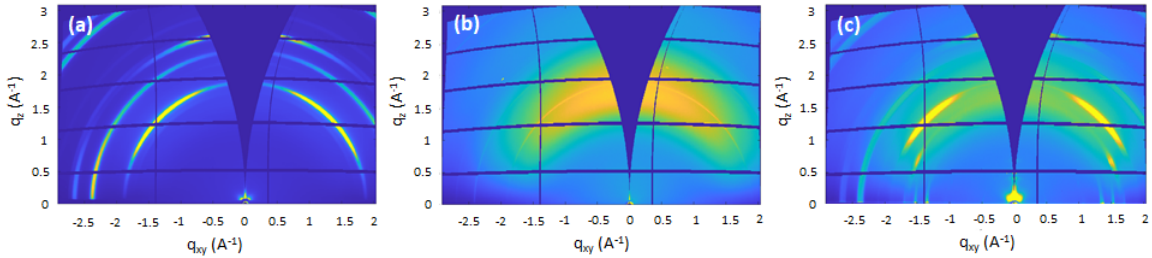


Figure 4.14: GIWAXS patterns of different device substrates used as internal marker: (a) FTO, (b) FTO/PEDOT:PSS, and (c) FTO/PEG+IL.

In the FTO case it was found a tetragonal structure with (200) as main crystallographic orientation (called texturing). On the contrary, PEDOT:PSS showed an halo indicating an amorphous structure. In the PEG+IL case the FTO signal is visible but there is also the appearing of an arc that was not visible in the FTO. At the same time, also the halo of an amorphous structure can be noticed. At room temperature PEG is a crystalline solid but the heating (during the solution preparation and the deposition

process), and the introduction of a certain percentage of IL could probably induce the transition to amorphous phase.

4.4.1 Reference configuration: FTO/PEDOT:PSS/MAPI

In Figure 4.15, the GIWAXS signals for the reference memristor configuration are represented, while Figure 4.16 shows the intensity of the signal integrated over the whole q space.

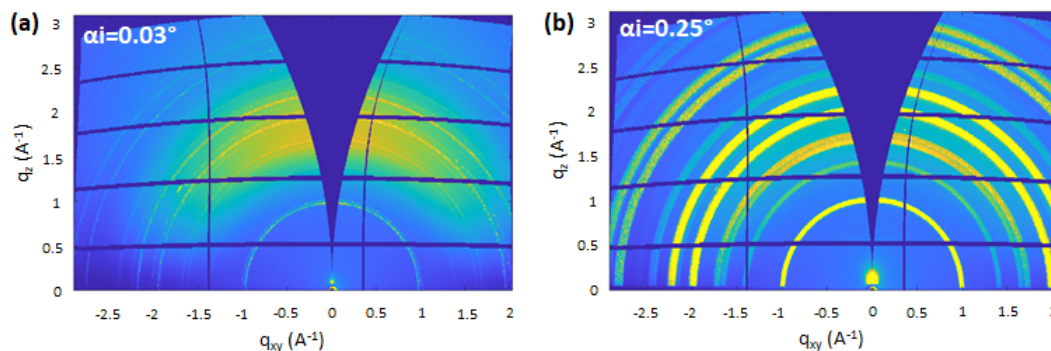


Figure 4.15: GIWAXS patterns in q -space of the sample FTO/PEDOT:PSS/MAPI for incidence angles α_i (a) smaller and (b) greater than α_c .

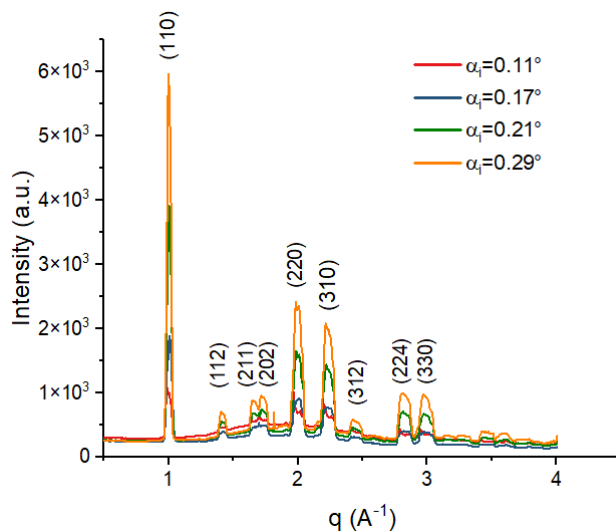


Figure 4.16: Integrated intensity profiles for different incidence angles α_i on the FTO/PEDOT:PSS/MAPI sample.

For small angles there is an amorphous structure (indicated by a "bulge" in the integrated intensity profiles) whose intensity decreases with the increasing of the angle. The structure exhibited by the perovskite is the tetragonal one and it is maintained across the whole thickness.

Figure 4.18 shows the the scattering patterns in polar space. In 4.18(a) is represented the rectangle, around the (110) peak, on which the integration to obtain the azimuthal profiles has been performed (Figure 4.18).

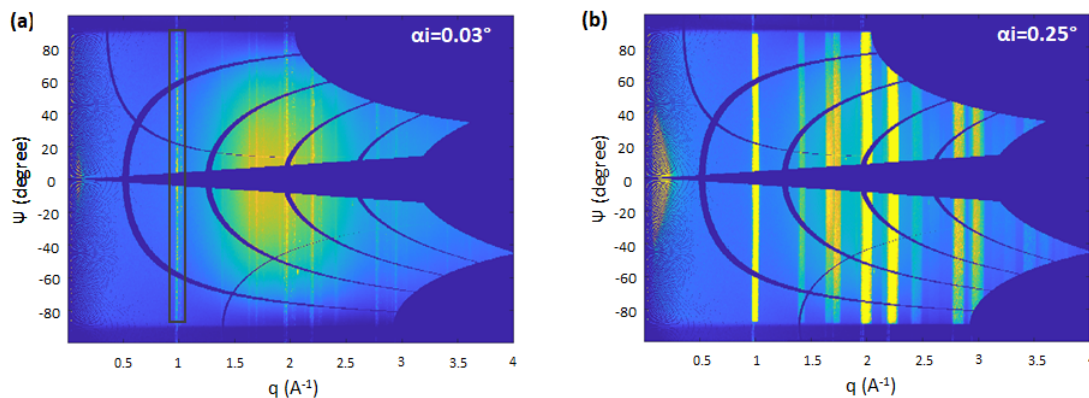


Figure 4.17: GIWAXS patterns in polar space of the sample FTO/PEDOT:PSS/MAPI for incidence angles α_i (a) smaller and (b) greater than α_c .

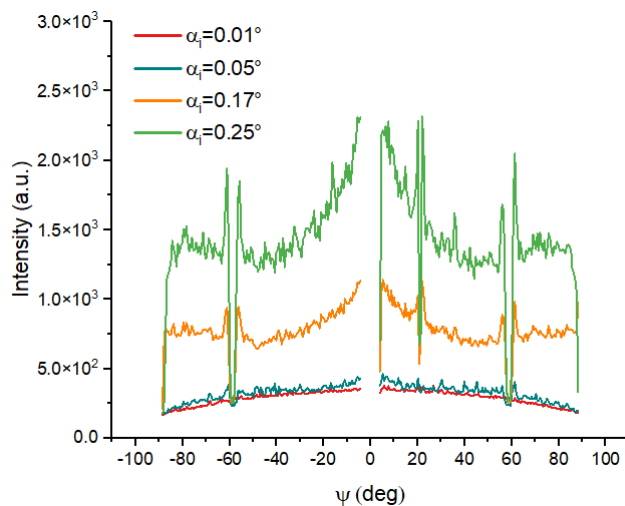


Figure 4.18: Azimuthal intensity profiles of the (110) peak for the sample FTO/PEDOT:PSS/MAPI with varying α_i .

The azimuthal profiles allow to understand that MAPI has a specific texturing, so it

is not random oriented as the uniform intensity over the rings could suggest. The higher intensity is centered at zero, indicating (110) as main crystallographic orientation.

4.4.2 Bottom configuration: FTO/PEG+IL/MAPI

In the case of the bottom device configuration, Figures 4.19 and 4.20 show that the structure is still the one found in the reference configuration, and also in this sample the tetragonal phase is maintained across the whole thickness

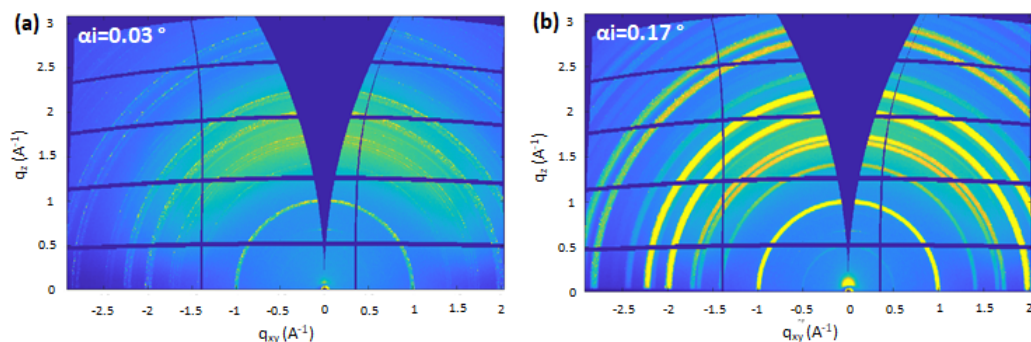


Figure 4.19: GIWAXS patterns in q -space of the sample FTO/PEG+IL/MAPI for incidence angles α_i (a) smaller and (b) greater than α_c .

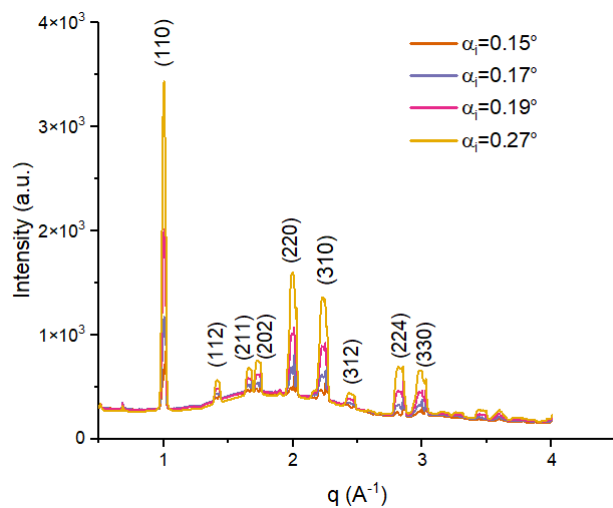


Figure 4.20: Integrated intensity profiles for different incidence angles α_i on the FTO/PEG+IL/MAPI sample.

From the azimuthal profiles (Figure 4.22), obtained integrating the region around the (110) peak as illustrated in Figure 4.21, a different intensity distribution with respect to the reference case can be noticed. It is more uniform for small angles, when the MAPI signal is predominant, while for greater angles two lateral peaks, representative of FTO, appear.

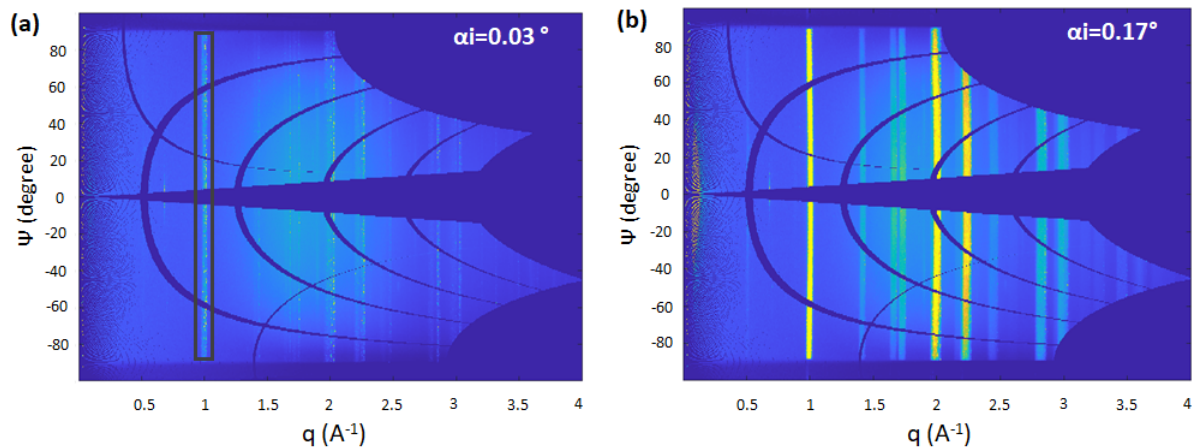


Figure 4.21: GIWAXS patterns in polar space of the sample FTO/PEG+IL/MAPI for incidence angles α_i (a) smaller and (b) greater than α_c .

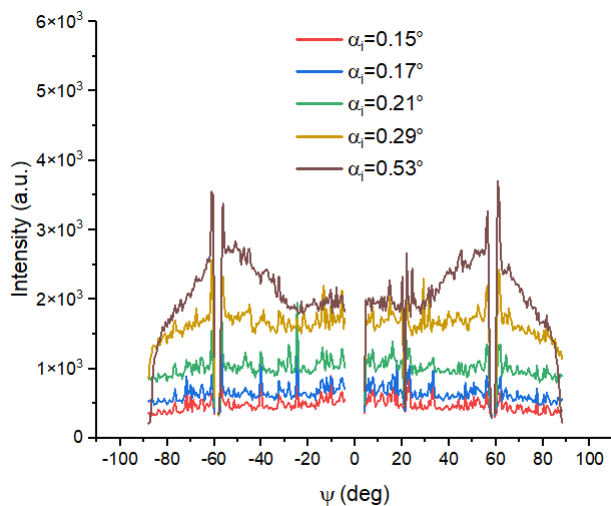


Figure 4.22: Azimuthal intensity profiles of the (110) peak for the sample FTO/PEG+IL/MAPI with varying α_i .

4.4.3 Top configuration: FTO/PEDOT:PSS/MAPI/PEG+IL

In the sample representing the top memristor configuration, the material appears deeply different from the previous two cases. Two main contributions are visible in the characteristic patterns in q space (Figure 4.23). One exhibits an high orientation and does not corresponds to MAPI(Figure 4.23(a)). The second component seems more random oriented and its signal became predominant increasing α_i (Figure 4.23(b) and 4.23(c)). As confirmation, in the integrated intensity profiles the peaks that were visible in the reference and bottom configurations are not present.

A possibility is that isopropanol, the solvent used for the buffer layer, degrades MAPI which subsequently undergoes a restructuring process with the PEG+IL layer, as already suggested by the sem images (Figure 4.5(c) and 4.5(d)). The structure which likely forms is $(\text{IL})_x(\text{MA})_{1-x}\text{PbI}_y$, determined mainly by the ratio between IL and MA.

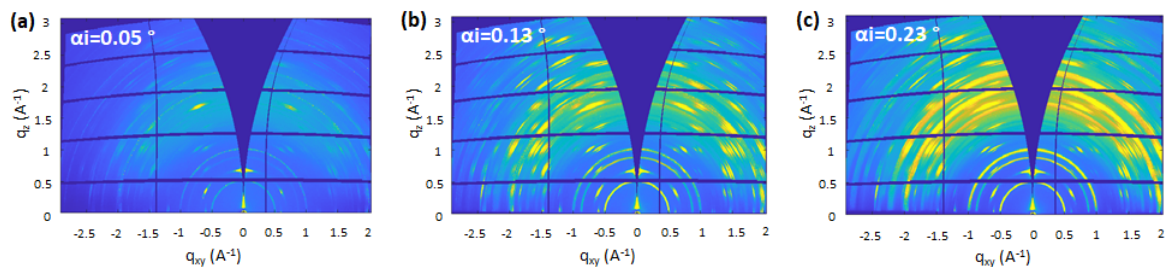


Figure 4.23: GIWAXS patterns in q -space of the sample FTO/PEDOT:PSS/MAPI/PEG+IL for incidence angles α_i (a) smaller and (b) greater than α_c .

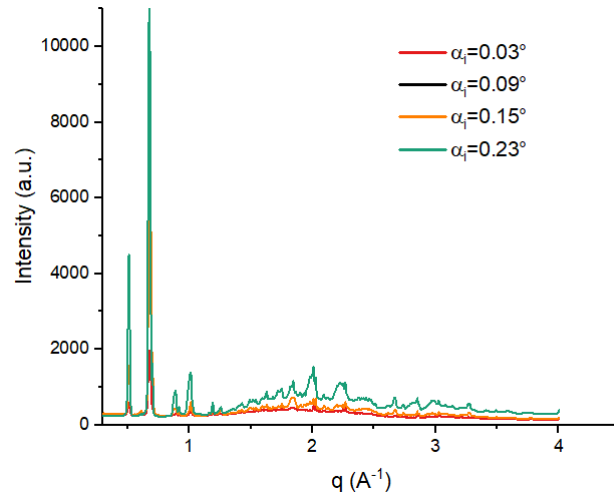


Figure 4.24: Integrated intensity profiles for different incidence angles α_i on the FTO/PE-DOT:PSS/MAPI/PEG+IL sample.

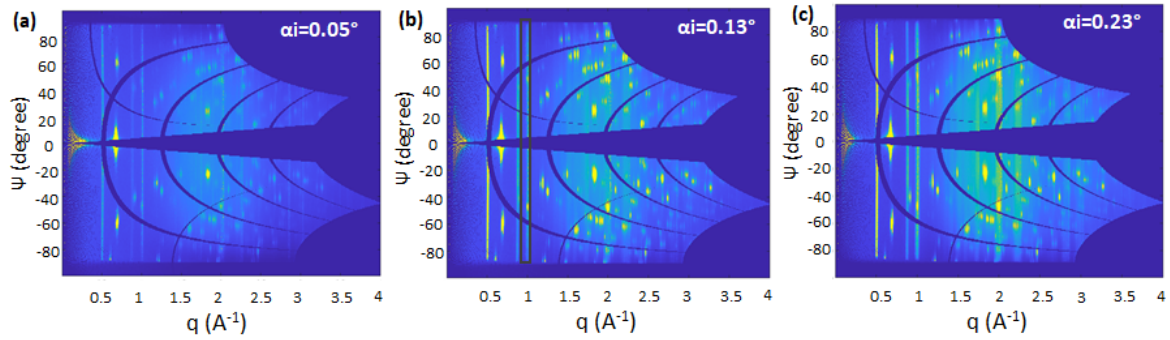


Figure 4.25: GIWAXS patterns in polar space of the sample FTO/PE-DOT:PSS/MAPI/PEG+IL for incidence angles α_i (a) smaller and (b) greater than α_c .

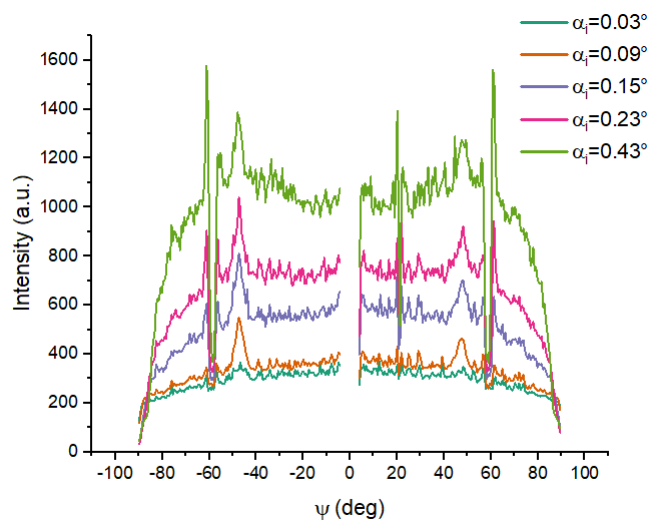


Figure 4.26: Azimuthal intensity profiles of the (110) peak for the sample FTO/PE-DOT:PSS/MAPI/PEG+IL with varying α_i .

Figure 4.25 and 4.26 show the characteristic patterns in polar space and the azimuthal profiles, respectively. However, further analysis are necessary in order to understand exactly how MAPI is modified and which kind of structure is formed.

Conclusions

Understanding the underlying mechanisms governing the hysteretic effect in perovskite-based devices is fundamental in order to have a complete picture of the complex interplay among the dynamic carrier and ionic transport under device operation. This would allow to tailor optoelectronic properties of perovskite-based memristor for specific applications, ranging from synaptic hardware to photosynaptic devices.

The purpose of this work was to study the effect of the integration of an ionic buffer layer in an already known memristor configuration to test how to control the electrical response. To do so, the conditions for obtaining an omogeneous buffer layer have been tested, recognizing as optimal options: 15% of ionic liquid concentration, 200 rpm for spin-coating speed, and dynamic deposition method. The insertion of the ionic layer into the device, in both top and bottom configurations, has demonstrated two different types of device activation. In the bottom case, the ON/OFF ratio is higher compared to the reference, but only in the first cycle, after which the device cannot be reset. In the top case, a change in polarity in the activation of the memristor was achieved. In both cases, reproducibility was confirmed for different contacts of the same device and for different devices. Furthermore, from the analysis conducted through GIWAXS measurements, it emerged that in the bottom case, the perovskite assumes a different orientation without undergoing structural changes due to the presence of the ionic layer. On the contrary, the top case is particularly interesting, as the obtained structure is no longer the MAPbI_3 , but has undergone a reconfiguration due to the interaction with the buffer layer.

It should be underlined that the memristor configurations tested in this work were designed specifically to study the possibility of manipulating the hysteretic response of the device. What remains unclear at this point is which kind of perovskite structure is formed in the top configuration and a clear description of the transport mechanism that leads to the different polarity of the device activation and the impossibility to switch off the bottom device. Hence, the principal analysis to perform, as continuation of this work, should be impedance spectroscopy measurements. Moreover, devices can be realized with strict control of the stoichiometry and varying the concentration of ionic liquid in the system. In this way, from the combination of GIWAXS results and I-V response, a correlation between the electrical behaviour and the structure can be determined.

Bibliography

- [1] Di Ventra, Massimiliano, and Yuriy V. Pershin. "On the physical properties of memristive, memcapacitive and meminductive systems." *Nanotechnology* 24.25 (2013): 255201.
- [2] Pershin, Yuriy V., and Massimiliano Di Ventra. "Memory effects in complex materials and nanoscale systems." *Advances in Physics* 60.2 (2011): 145-227.
- [3] Bisquert, Juan, and Antonio Guerrero. "Chemical inductor." *Journal of the American Chemical Society* 144.13 (2022): 5996-6009.
- [4] Gonzales, Cedric Title Hysteresis Control in Hybrid Perovskite-based Devices for Photovoltaic and Neuromorphic Computing Applications, Universitat Jaume I (2023).
- [5] Arndt, Benedikt, et al. "Spectroscopic indications of tunnel barrier charging as the switching mechanism in memristive devices." *Advanced functional materials* 27.45 (2017): 1702282.
- [6] Mannocci, P., et al. "In-memory computing with emerging memory devices: Status and outlook." *APL Machine Learning* 1.1 (2023).
- [7] Ielmini, Daniele, and Stefano Ambrogio. "Emerging neuromorphic devices." *Nanotechnology* 31.9 (2019): 092001.
- [8] Kozma, Robert, Robinson E. Pino, and Giovanni E. Paziienza, eds. *Advances in neuromorphic memristor science and applications*. Vol. 4. Springer Science & Business Media, 2012.
- [9] Snaith, Henry J. "Perovskites: the emergence of a new era for low-cost, high-efficiency solar cells." *The journal of physical chemistry letters* 4.21 (2013): 3623-3630.
- [10] Maggiora, Joshua, Feng Li, and Rongkun Zheng. "Charge Transport Properties of Methylammonium Lead Trihalide Hybrid Perovskite Bulk Single Crystals." *physica status solidi (RRL)–Rapid Research Letters* 15.1 (2021): 2000410.

- [11] Khan, Imran, et al., eds. Hybrid Perovskite Composite Materials: Design to Applications. Woodhead Publishing, 2020.
- [12] Zhang, Yurou, et al. "Halide perovskite single crystals: Optoelectronic applications and strategical approaches." *Energies* 13.16 (2020): 4250.
- [13] Fujiwara, Hiroyuki, ed. Hybrid Perovskite Solar Cells: Characteristics and Operation. John Wiley & Sons, 2021.
- [14] Poglitsch, Albrecht, and Daniel Weber. "Dynamic disorder in methylammoniumtrihalogenoplumbates (II) observed by millimeter-wave spectroscopy." *The Journal of chemical physics* 87.11 (1987): 6373-6378.
- [15] Kieslich, Gregor, Shijing Sun, and Anthony K. Cheetham. "Solid-state principles applied to organic–inorganic perovskites: new tricks for an old dog." *Chemical Science* 5.12 (2014): 4712-4715.
- [16] Eames, Christopher, et al. "Ionic transport in hybrid lead iodide perovskite solar cells." *Nature communications* 6.1 (2015): 7497.
- [17] Sayantan Mazumdar, Ying Zhao, and Xiaodan Zhang. Stability of perovskite solar cells: Degradation mechanisms and remedies. *Frontiers in Electronics*, page 8, 2021.
- [18] Asghar, Muhammad I., et al. "Device stability of perovskite solar cells—A review." *Renewable and Sustainable Energy Reviews* 77 (2017): 131-146.
- [19] Ouyang, Yixin, et al. "Photo-oxidative degradation of methylammonium lead iodide perovskite: mechanism and protection." *Journal of Materials Chemistry A* 7.5 (2019): 2275-2282.
- [20] Satapathi, Soumitra, Kanishka Raj, and Mohammad Adil Afroz. "Halide-perovskite-based memristor devices and their application in neuromorphic computing." *Physical Review Applied* 18.1 (2022): 017001.
- [21] Covi, Erika, et al. "Switching dynamics of Ag-based filamentary volatile resistive switching devices—Part I: Experimental characterization." *IEEE Transactions on Electron Devices* 68.9 (2021): 4335-4341.
- [22] Wang, Yan, et al. "Synergies of electrochemical metallization and valence change in all-inorganic perovskite quantum dots for resistive switching." *Advanced materials* 30.28 (2018): 1800327.
- [23] Ielmini, D., Z. Wang, and Y. Liu. "Brain-inspired computing via memory device physics." *APL Materials* 9.5 (2021).

- [24] Deng, Wei, et al. "Organic molecular crystal-based photosynaptic devices for an artificial visual-perception system." *NPG Asia Materials* 11.1 (2019): 77.
- [25] Xue, Zhigang, Dan He, and Xiaolin Xie. "Poly (ethylene oxide)-based electrolytes for lithium-ion batteries." *Journal of Materials Chemistry A* 3.38 (2015): 19218-19253.
- [26] Kennard, Rhiannon M., et al. "Ferroelastic hysteresis in thin films of methylammonium lead iodide." *Chemistry of Materials* 33.1 (2020): 298-309.
- [27] JEOL Application Data Sheet
- [28] Li, Cheng, et al. "Real-time observation of iodide ion migration in methylammonium lead halide Perovskites." *Small* 13.42 (2017): 1701711.
- [29] Santoro, G., et al. "Use of intermediate focus for grazing incidence small and wide angle x-ray scattering experiments at the beamline P03 of PETRA III, DESY." *Review of Scientific Instruments* 85.4 (2014).
- [30] Steele, Julian A., et al. "How to GIWAXS: Grazing Incidence Wide Angle X-Ray Scattering Applied to Metal Halide Perovskite Thin Films." *Advanced Energy Materials* (2023): 2300760.
- [31] Guerrero, Antonio, Juan Bisquert, and Germà Garcia-Belmonte. "Impedance spectroscopy of metal halide perovskite solar cells from the perspective of equivalent circuits." *Chemical Reviews* 121.23 (2021): 14430-14484.
- [32] Bou, Agustin, and Juan Bisquert. "Impedance spectroscopy dynamics of biological neural elements: from memristors to neurons and synapses." *The Journal of Physical Chemistry B* 125.35 (2021): 9934-9949.
- [33] Berruet, Mariana, et al. "Physical model for the current–voltage hysteresis and impedance of halide perovskite memristors." *ACS Energy Letters* 7.3 (2022): 1214-1222.
- [34] Marronnier, Arthur, et al. "Electrical and optical degradation study of methylammonium-based perovskite materials under ambient conditions." *Solar Energy Materials and Solar Cells* 178 (2018): 179-185.
- [35] X-Ray Optics Calculator, <http://purple.iptm.ru/xcalc/xcalcmysql/refindex.php>
- [36] Ke, Chun-Ren, et al. "Air-stable methylammonium lead iodide perovskite thin films fabricated via aerosol-assisted chemical vapor deposition from a pseudohalide Pb (SCN) 2 precursor." *ACS Applied Energy Materials* 2.8 (2019): 6012-6022.